Journal of Nanobiotechnology

RESEARCH

Open Access

MiR-100-5p-rich small extracellular vesicles from activated neuron to aggravate microglial activation and neuronal activity after stroke

Danqing Xin[1†], Tingting Li[1†], Yijing Zhao[1†], Xiaofan Guo[2], Chengcheng Gai[1], Zige Jiang[1], Shuwen Yu[3], Jiao Cheng[3], Yan Song[1], Yahong Cheng[1], Qian Luo[3], Bing Gu[3], Dexiang Liu[3] and Zhen Wang[1*]

Abstract

Ischemic stroke is a common cause of mortality and severe disability in human and currently lacks effective treatment. Neuronal activation and neuroinflammation are the major two causes of neuronal damage. However, little is known about the connection of these two phenomena. This study uses middle cerebral artery occlusion mouse model and chemogenetic techniques to study the underlying mechanisms of neuronal excitotoxicity and severe neuroinflammation after ischemic stroke. Chemogenetic inhibition of neuronal activity in ipsilesional M1 alleviates infarct area and neuroinflammation, and improves motor recovery in ischemia mice. This study identifies that ischemic challenge triggers neuron to produce unique small extracellular vesicles (EVs) to aberrantly activate adjacent neurons which enlarge the neuron damage range. Importantly, these EVs also drive microglia activation to exacerbate neuroinflammation. Mechanistically, EVs from ischemia-evoked neuronal activity induce neuronal apoptosis and innate immune responses by transferring higher miR-100-5p to adjacent neuron and microglia. MiR-100-5p can bind to and activate TLR7 through $U_{18}U_{19}G_{20}$-motif, thereby activating NF-κB pathway. Furthermore, knock-down of miR-100-5p expression improves poststroke outcomes in mice. Taken together, this study suggests that the combination of inhibiting aberrant neuronal activity and the secretion of specific EVs-miRNAs may serve as novel methods for stroke treatment.

Keywords Neuronal activity, Small extracellular vesicles, MiR-100-5p, Microglial activation, Stroke

†Danqing Xin, Tingting Li, and Yijing Zhao have contributed equally to this work.

*Correspondence:
Zhen Wang
wangzhen@sdu.edu.cn
Full list of author information is available at the end of the article

Graphical Abstract

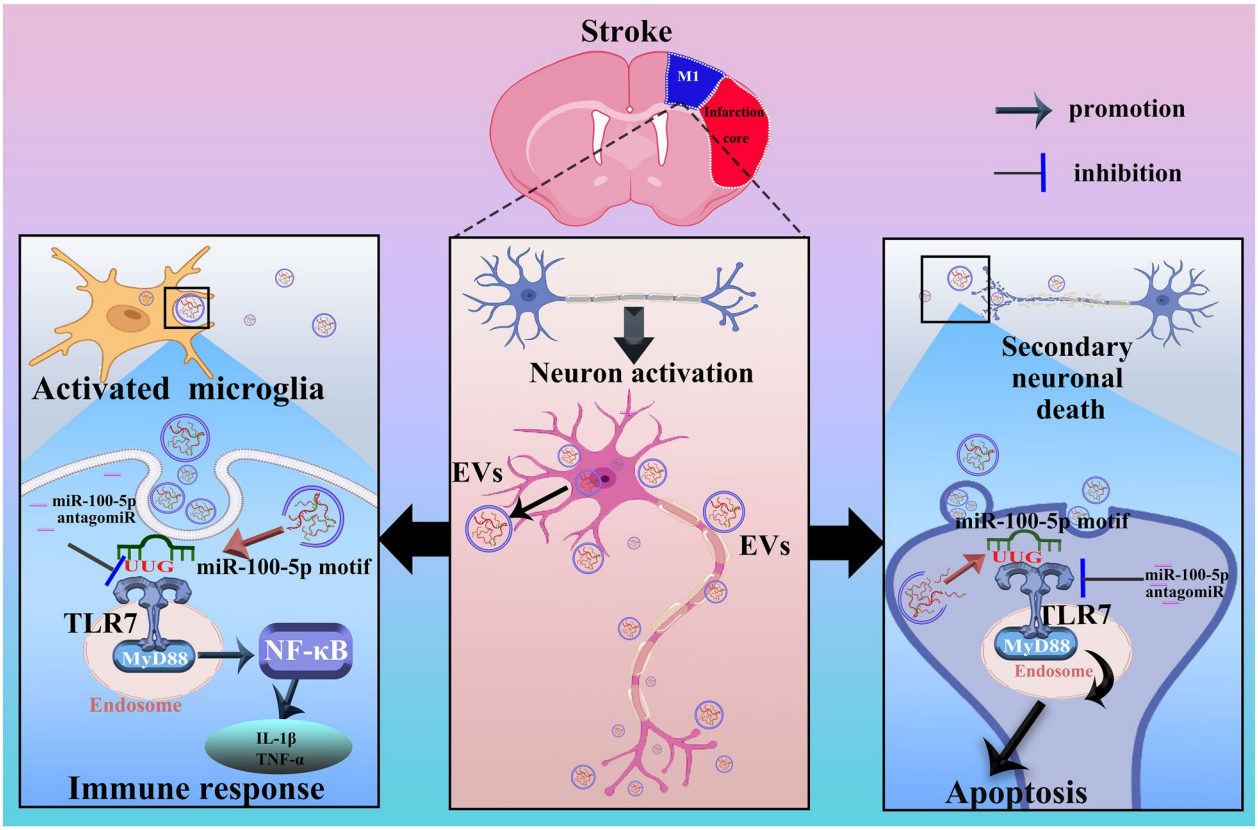

Background

Ischemic stroke due to insufficient blood supply to the brain caused by energy metabolism disorders, membrane depolarization, excitatory amino acids (such as glutamate and aspartic acid) massive release and ionic imbalance, resulting in rapid neuronal cell death in the ischemic core and the potential for progressive cell death in the penumbra [1]. In the acute phase after stroke, abnormal neuronal activity is considered to be an important factor leading to the formation and spread of infarction [2, 3]. During this acute phase of ischemia, cortical neuronal activation is required for somatosensory stimulation to trigger peri-infarct depolarizations [4]. Ischemic stroke, the depolarization of neurons and glial cells leads to the release of K^+ and glutamate from cells. The increase of extracellular K^+ and glutamate levels can stimulate the depolarization of cells in the penumbra around the infarct. This repeated depolarization is called peri-infarct depolarization. Peri-infarct depolarization can trigger peri-infarct depolarization, causing the infarct core to expand to the penumbral region, leading to the enlargement of the infarct focus [5]. Microglia are major determinants of the peri-infarct environment and exert important effects upon the development of neuroinflammation [6]. Manipulations of glial cells in the peri-infarct tissue have the potential to improve or impair functional recovery resulting from stroke. However, little is known regarding the connections between neuronal activation and neuroinflammation [7, 8].

Approaches involved with altering neuronal activity, such as anodal direct current stimulation or transcranial magnetic stimulation, have been shown to enhance motor performance after stroke [9–11]. In rodent models of stroke, pharmacogenetic treatments, designer receptors exclusively activated by designer drugs (DREADDs)-based chemogenetic approach, and optogenetics that enhance neuronal activity in peri-infarct cortex adjacent to the stroke also promote motor recovery [12–14]. Moreover, acute inhibition within a subset of excitatory neurons with after ischemic stroke can prevent brain injury and improve functional outcomes in mice [7]. These data suggest that a distinct involvement of activity

within different neuronal subsets is critically involved in contributing to stroke pathogenesis. In this report, we first identify the state of excitability within different neuronal subsets in the primary motor cortex (M1) following stroke and then determine whether pharmacogenetic manipulations would be capable of modifying this neuronal activity to restore functional recovery under conditions of ischemia-induced stroke.

Small extracellular vesicles (EVs, 30–150 nm in diameters) are secreted by almost all cell types involved in intercellular communication [15, 16]. EVs have a lipid bilayer structure, carrying biologically active molecules such as nucleic acids, proteins, and lipids, which can achieve material exchange between cells, which not only participate in the regulation of cell proliferation and survival, but also play an important role in signal transduction and cell communication [17]. In the central nervous system (CNS), EVs can be released from all cell types including microglia [18], astrocytes [19], and neurons [20], and participate in communication between neurons and glial cells [21, 22]. Specifically, EVs derived from cultured neurons in vitro can be internalized by microglia [23] and neuron-derived EVs containing miR-21-5p promote proinflammatory activation of microglia and inhibit neurite outgrowth [23]. On the contrary, another study found that neuron-derived EVs promote functional behavioral recovery following injured spinal cord of mice by suppressing the activation of M1 microglia and A1 astrocytes [24]. EVs derived from neuron can be internalized in microglia and suppress lipopolysaccharide (LPS)-induced microglia activation [25]. Results from a previous report have revealed that EVs can be released from cultured neurons in an activity-dependent manner [26]. In stroke, the role of neuronal activity and even more so in EVs-miRNA as well as the underlying mechanisms still remain elusive.

In this report, we tested our hypothesis that EVs released in response to ischemia-evoked neuronal activity may be relevant to mechanisms involved with poststroke microglial activation and neuronal injury. Our results revealed that in response to "ischemia-evoked neuronal activity", EVs possessed aberrant expressions of specific miRNAs that can compromise cell survival and balance of the immune environment, as demonstrated under conditions of both in vivo cerebral ischemia and in vitro oxygen-glucose-deprivation/reoxygenation (OGD/R).

Material and methods

Ethics

All animal care and experimental procedures were conducted in accordance with the guidance of the Care and Use of Laboratory Animals from the National Institutes of Health and were approved by the Laboratory Animal Ethics Committee of Shandong University (approval No. ECSBMSSDU2022-2–52). Participants who worked with the animal models were trained following Institutional Animal Care and Use Committee Guidebook rules to reduce the usage and mortality of experimental animals.

Surgery

Eight-week-old male C57BL/6 mice were purchased from Beijing Vital River Laboratory Animal Technology Co., Ltd. (Beijing, China).

Transient focal cerebral ischemia was induced by middle cerebral artery occlusion (MCAO), which was established as previously described [27]. After isoflurane anesthesia (5% for induction; 1% for maintenance), the right middle cerebral artery was blocked by inserting the monofilament (Rayworld Life Technology Co., Ltd., Shenzhen, China, MSMC21B120PK50) into the right internal carotid artery. The body temperature was sustained at 37 °C with a heated blanket throughout the procedure. Indicated time (30 min, 1 h or 2 h) after occlusion, reperfusion was allowed by removing monofilament. Unless otherwise indicated, the ischemic time was 2 h. In addition to inserting monofilament, Sham group went through the same process. The exclusion criteria included mice showing no depressed signs or alteration in movements after awakening from anesthesia. No significant adverse effects were observed in viral vector-treated mice.

Models that meet the following criteria are considered successful: (1) Delayed or disappeared pain retraction in the opposite limb; (2) When hanging upside down, the opposite upper limb flexes towards the chest; (3) When walking, the body tilts or rotates to the opposite side; (4) Homer's syndrome appear on the opposite side [28].

Stereotaxic surgery

DREADDs belong to a class of chemogenetically engineered proteins that are based on G protein-coupled receptors. DREADDs can be activated or silenced by small molecule actuators such as clozapine-N-oxide (CNO). For the chemicalgenetics experiment, AAV9-hSyn-HA-hM3(Gq)-IRES-mCitrine (hM3Dq, 9.04×10^{13} v.g/mL), AAV9-hSyn-HA-hM4(Gi)-IRES-mCitrine (hM4Di, 1.29×10^{13} v.g/mL) were purchased from Shanghai Genechem Co., Ltd (Shanghai, China). The hM4Di is commonly used to inhibit neuronal activity. The hM3Dq is commonly used to increased neuronal activity. Vector injection Surgeries were performed under aseptic conditions. Stereotaxic injections of purified high titer hM3Dq, or hM4Di were diluted with phosphate-buffered saline (PBS) and injected 2×10^{9} v.g/2 μL. To cover the entire M1, mice were microinjected in right hemisphere using the following coordinates: [from bregma: anteroposterior

(AP) + 1.0 mm, mediolateral (ML) + 1.5 mm, dorsoventral (DV) −1.0 mm)], using a 10 μL Hamilton syringe (Shanghai Gaoge Industry & Trade Co., Ltd., Shanghai, China). The injection speed was set at 0.2 μL/min. After each injection, the needle remained in situ for 5 min to minimize backflow along the needle. Two weeks prior to surgery, viral injection (hM4Di and hM3Dq) was performed under anesthesia.

To obtain direct evidence that miR-100-5p enriched EVs induced brain damage following stoke, PBS, EVs from normal neurons (referred to as Nor-N-EVs) or OGD/R-exposed neurons (referred to as OGD-N-EVs) were injected into the M1 by stereotactic injection. Here, we chose a milder form of stress (30 min occlusion) to better distinguish the miR-100-5p increase on brain damage.

For miR-100-5p functional loss experiments, miR-100-5p antagomiR (miR-100-5p^{anta}) and control antagomiR (control^{anta}) were purchased from Shanghai Genechem Co., Ltd (Shanghai, China). Vector injection Surgeries were performed under aseptic conditions. Two days prior to MCAO, miR-100-5p^{anta} or control^{anta} (100 pmol/2 μL) was dissolved in PBS and injected into the right intracerebroventricular (coordinates: AP-0.3 mm, ML + 1.0 mm, and DV-3.0 mm). The solution was delivered at a rate of 0.2 μL/min. After each injection, the needle remained in situ for 5 min to minimize backflow along the needle.

Chronic CNO injections

CNO was dissolved in dimethyl sulfoxide (DMSO) and then diluted in 0.9% saline to yield a final DMSO concentration of 0.5%. Saline solution for control injections also consisted of 0.5% DMSO. The intraperitoneal (i.p.) injection of CNO or Vehicle (1 mg/kg) was administered in conscious mice for 5 times. CNO or Vehicle (once every 24 h, 3 times in total) was injected intraperitoneally 3 days before MCAO. The fourth injection of CNO or Vehicle was administered at 30 min before MCAO. The last injection of CNO or Vehicle was administered at 23.5 h after MCAO. The chosen doses of CNO did not induce any behavioral signs of seizure activity (data not shown here). At 24 h post-surgery, the tissues were collected for next experiment.

Regarding the activation method of CNO, we refer to previous studies to choose chronic CNO activation [12].

Behavioral assessment

Modified neurological severity score

The modified neurological severity score (mNSS) was used to evaluate neurological function [29]. The total score ranges from 0 to 18 points, and a higher score indicates a more severe neurological deficit. The mNSS test was performed 24 h after MCAO.

Negative geotaxis test

The negative geotaxis test was used to assess bilateral asymmetry. Mice were placed in a standard position, head downward, on an elevated 45° inclined board (15 cm × 30 cm) to turn 180° and crawl up the board [30]. When quitting the standard position, any leftward or rightward rotation was recorded. The test was conducted 3 times per mouse, and the average time was obtained. A 60-s time out was used. Mice that fell or failed to turn were not counted.

Kondziella's inverted screen test

The mouse was placed in the center of the wire mesh screen before the screen was rotated to an inverted position slowly over 3 s, with the mouse's head declining first. When the screen was stable and standing on all four legs, the timer was started. The time when the mouse fell off was noted, or the mouse was removed when the criterion time of 5 min maximum was reached.

The grid walking test

Grid walking test was performed to assess motor coordination deficits after ischemic stroke. Each mouse was placed in the middle of a raised metal square-shaped frame grid unit and allowed to walk freely for 5 min. In the process of walking, the left foot stepped into the square, which was identified as foot slip. At rest, the grid was at the height of the left foot, which was also considered to be foot slip. The 75% ethanol was used to clean the grid after each trial. The camera (iPhone 12, USA) was placed 40 cm below the wire mesh to capture the number of foot slip. The collected videos were analyzed in slow motion (1/5 real-time speed) by experimenters who didn't know about experimental grouping. Calculate the left forelimb missed falls rate: footstep error = left forelimb missed falls times/(left forelimb missed falls times + left forelimb not missed falls times) × 100%. Before MCAO surgery, no obvious difference was observed all mice in grid walking test (data not shown).

Isolation and identification of EVs

We referred to previous studies to obtain EVs-depleted fetal bovine serum (FBS) using ultra-high speed centrifugation [31]. The FBS was depleted of EVs by ultracentrifugation at 100,000 × g for 18 h at 4 °C. After that, filter the supernatant with 0.22 μm to obtain sterile EVs-depleted FBS. The extraction method for EVs from cell culture medium of PC12 cell (the neuronal cell line) was performed as previously described [32]. The detailed method for proposing Nor-N-EVs and OGD-N-EVs were

as follows: 5×10^6 PC12 cells were inoculated with 20 mL of RPMI-1640 medium supplemented with 10% FBS, 1% penicillin–streptomycin in a T175 cm^2 cell culture flasks, when the cell density reached 70%, the cells were cultured in EVs-depleted FBS-containing RPIM 1640 medium for 12 h, and then 200 mL of medium was collected for EVs extraction by differential centrifugation at 4℃ as follows: 300×g for 10 min, 2,000×g for 10 min, 10,000×g for 30 min, 100,000×g for 70 min, 100,000×g for 70 min, and then the pellet was resuspended in PBS, finally, Nor-N-EVs were obtained.

The 5×10^6 PC12 cells were inoculated with 20 mL of RPMI-1640 medium supplemented with 10% FBS, 1% penicillin–streptomycin in a T175 cm^2 cell culture flasks. When the cell density reached 70%, the cells were cultured in glucose-free RPIM 1640 medium under hypoxic conditions (1% O_2, 5% CO_2, and 94% N_2) for 6 h. The cells were then incubated under a humidified atmosphere containing 5% CO_2 in EVs-depleted FBS-containing RPIM 1640 medium with or without 20 μM GW4869 for 12 h, and 200 mL of medium was collected. OGD-N-EVs or OGD-N-EVs + GW4869 were finally obtained by following the centrifugation steps of Nor-N-EVs.

Regarding the extraction of EVs from M1, a total of 40 mice (5 mice in a pool, each group have 4 pool) were used to extract EVs for miRNA sequencing. The method for extraction of EVs from M1 was as follows: the M1 was chopped until homogenization, and the homogenate was placed in a test tube containing 2 mg/mL collagenase and 40 U/mL DNase I for 30 min at 37 °C. The homogenate was filtered through 70 μm cell strainers and then centrifuged at 300×g for 10 min, 2,000×g for 10 min, 10,000×g for 30 min, 100,000×g for 70 min, and then the pellet was resuspended in PBS and stored at − 80 °C until further experiments.

The extracted EVs were quantitatively analyzed using bicinchoninic acid assay and used for subsequent research.

To observe the morphology of the acquired EVs derived from neuron (N-EVs) in vitro or brain tissue in vivo (M1-EVs), transmission electron microscopy (TEM; Tecnai 12; Philips, Best, The Netherlands) and ZetaView (Particle Metrix, Germany) were used to evaluate the diameter distribution. Specific surface markers, including CD9, CD63 and Calnexin were also detected by Western blot.

MiRNA sequencing

The differentially expressed miRNA level in the M1-EVs was screened by Novogene Bioinformatics Technology Co. (Beijing, China). Total RNA detection, gene library construction, and HiSeq/MiSeq sequencing were carried out according to the manufacturer's instructions. To obtain miRNA profiles that differently distributed in EVs of Sham and MCAO, we set the fold change threshold of MCAO group at |log2 (Fold Change)| > 1 as compared to Sham group for further analysis. The differentially expressed miRNAs were determined using ANOVA.

EVs labeled with CD63 or PKH67

The pCMV-EGFP-CD63-Neo (CD63) plasmids were produced by Wuhan Miaoling biology science and technology co., ltd (Wuhan, China). The PC12 cells were transduced with the CD63 plasmid using Lipofectamine 2000 (Invitrogen, Thermo Fisher Scientific, Grand Island, New York, USA) for 6 h, and then cultured for 48 h in RPMI-1640 medium supplemented with 10% FBS and 1% penicillin–streptomycin. After completion, RPMI 1640 complete culture with 10% EVs-depleted FBS was used for 12 h before collecting the cell supernatant. EVs isolation was performed as the above described. The purified EVs from normal neuron was referred to as Nor-N-EVs. Finally, CD63-labeled Nor-N-EVs were resuspended in PBS.

The PC12 cells were transduced with the CD63 plasmid using Lipofectamine 2000 for 6 h, and then cultured for 48 h in RPMI-1640 medium supplemented with 10% FBS and 1% penicillin–streptomycin, and then RPMI 1640 without-glucose medium was replaced and transferred to a three-gas incubator with 1% O_2, 5% CO_2 and 94% N_2 for 6 h. After completion, replaced RPMI 1640 complete culture with 10% EVs-depleted FBS and incubated it in a normal incubator for 12 h before collecting the cell supernatant. The purified EVs from OGD/R-exposed neuron (referred to as OGD-N-EVs). CD63-labeled OGD-N-EVs were extracted by ultracentrifugation.

PKH67 (Sigma-Aldrich Co., St Louis, MO, USA) was used to mark the EVs according to the manufacturers' direction. Briefly, PKH67 dye (4 μL) was mixed into Diluent C (1 mL) to obtain the PKH67 solution. Then, PKH67 solution (1 mL) and diluent EVs (1 mL) were combined within centrifugation tube for 5 min, 2 mL 1% bovine serum albumin was added to centrifugation tube to stop dyeing. Then, the mixture was ultracentrifuged (100,000×g) for 70 min to obtain EVs precipitate, followed by washing again with PBS (100,000×g) for 70 min. Finally, PKH67-labeled EVs were resuspended in PBS. The PKH67-only was taken as a control to investigate the uptake of EVs by recipient cells. The acquisition of PKH67-only is consistent with PKH67-labeled EVs, except for the absence of EVs.

Cell transfection

PC12 cells, BV-2 cells and primary cortical neurons were treated with miR-100-5p mimics (50 nM), miR-100-5p mutant (50 nM) or negative control (NC) (50 nM) using

Lipofectamine 2000 for 6 h, and then cultured for 48 h in complete medium to collect cells for subsequent research.

PC12 cells and BV-2 cells were treated with TLR7 siRNA (50 nM) or Control siRNA (50 nM) using Lipofectamine 2000 for 6 h, and then cultured for 48 h in complete medium to collect cells for subsequent research.

PC12 cells and BV-2 cells were treated with NC (50 nM) + TLR7 siRNA (50 nM) or miR-100-5p mimics (50 nM) + TLR7 siRNA (50 nM) using Lipofectamine 2000 for 6 h, and then cultured for 48 h in complete medium to collect cells for subsequent research.

PC12 cells and primary cortical neurons were treated with pCMV-HA-hM3D(Gq)-EGFP-FRT-Hyg (hM3Dq)-plasmid (2 μg/mL) or pCMV-CMV-mCherry-hM4D(Gi)-3 × HA-Puro (hM4Di)-plasmid (2 μg/mL) using Lipofectamine 2000 for 6 h, and then cultured for 48 h in complete medium to collect cells for subsequent research.

Electrophysiology

Primary mouse cortical neurons were transfected with hM3Dq-plasmid or hM4Di-plasmid or miR-100-5p mimics or NC as described above. The firing of action potential in primary cortical neurons was recorded using perforated-cell recording in the current patch clamp mode. The data was acquired using HEKA EPC 10 USB and analyzed with patch master software (HEKA). Pipettes were pulled with the micropipette puller (P-97, Sutter) with a resistance of 3-5MΩ. The bath solution contains (in mM): 130 NaCl, 2 $CaCl_2$, 2 $MgCl_2$, 5 KCl, 10 HEPES, 10 glucose, and 10 sucrose, with pH = 7.4 adjusted by NaOH and osmolarity of 310 mOsm. The pipette solution contains (in mM): 140 K-gluconate, 5 HEPES, 0.5 EGTA, 2 $MgCl_2$, 0.1 $CaCl_2$, and 5 Na_2-ATP, with pH = 7.2 adjusted by KOH and osmolarity of 300 mOsm. Gramicidin (2.5 μg/mL) was used to perforate cell membranes in this study. All the cells were held at -60 mV initially if not specified.

Ca^{2+} concentration measurements

The concentration of intracellular Ca^{2+} was measured by the Fura-2 AM (S1052, Beyotime Biotechnology, China, Shanghai) according to the manufacturer's protocol. Fura-2 reagents (3 μM) were added to the cells, which were incubated for 30 min at 37 °C. They were then analyzed by a microplate reader at 340 nm and 380 nm, as previously described [33].

Fluorescence activated cell sorting of c-Fos-expressing neurons from brain tissue

Brains were rapidly extracted 6 h and 24 h after MCAO, M1 were cut in PBS containing 0.2% bovine serum albumin on ice. The tissue was digested with 0.25% trypsin to obtain single cells. Cell suspensions were pelleted and resuspended in PBS for sorting via fluorescence activated cell sorting (FACS) [34, 35]. The primary antibodies: c-Fos (E-8) FITC antibody (sc-166940 FITC), CaMKIIα (G-1) Alexa Fluor 680 antibody (sc-5306 AF680), GAD67 (F-6) PE antibody (sc-28376 PE) (Santa Cruz Biotechnology).

Immunoprecipitation assay

Immunoprecipitation (IP) assay was performed on HEK293T cells. Briefly, HEK293T cells transfected with miR-100-5p (50 nM)/miR-100-5p mut $G_6G_{20}U_7U_{18}U_{19}U_{21} \rightarrow AAAAAA$ (50 nM) and pCMV-EGFP-TLR7-Neo (TLR7) plasmid (2 μg/mL) were harvested 48 h post-transfection and lysed in NP-40 containing PMSF for 20 min on ice and centrifuged at 12,000 rpm for 15 min at 4 °C. Cell lysate supernatant was incubated with TLR7 antibody or IgG antibody at 4 °C overnight with rotation and then washed 4 times with NP-40 buffer. Then, the protein A + G beads were added to bond with antibody. The immunoprecipitated proteins with beads were centrifuged, washed three times with NP-40 buffer and analyzed by Western blot.

RNA immunoprecipitation assay

RNA immunoprecipitation (RIP) assay was used to determine the binding between TLR7 and miR-100-5p using Magna RIP™ RNA-Binding Protein Immunoprecipitation Kit (Gzscbio, Guangzhou, China). Briefly, HEK293T cells transfected with miR-100-5p (50 nM)/miR-100-5p mut $G_6G_{20}U_7U_{18}U_{19}U_{21} \rightarrow AAAAAA$ (50 nM) and TLR7 plasmid (2 μg/mL) and the level of miR-100-5p was detected using qRT-PCR.

Statistical analysis

All data are presented as mean ± standard deviation (SD), and each experiment was performed in triplicate at least. Data analysis was performed using IBM SPSS statistics 26.0 software. The Shapiro–wilk test was used to test whether the data conformed to the normal distribution. Normally distributed data were analyzed with the independent samples *t*-test (2 groups) or one-way or two-way ANOVA followed by the Bonferroni multiple comparisons test (details in figure legends). If it did not conform to the normal distribution, the Mann–Whitney U test was used between the two groups, and the Kruskal–Wallis test was used between multiple groups. Correlation was measured using Pearson correlation analysis. Statistical graphs are generated using GraphPad Prism 8.0.1. Statistical differences are presented at probability levels of $^{*}p < 0.05$, $^{**}p < 0.01$ and $^{***}p < 0.001$. All of the experiments were carried out in a blinded manner, and

experimenters were unaware of the treatment conditions and group assignment. Significant outliers were calculated using SPSS 26.0 software and were excluded from the statistical analysis.

The sample size was calculated in our pilot study to determine the smallest number of mice required to detect remarkable differences in the behavioral experiment between Sham and MCAO group. Using a power analysis (http://powerandsamplesize.com/Calculators/), it has been estimated that a sample size of 3 (mNSS) and 7 mice (negative geotaxis test) per group to detect a difference with a type I error (α) of 0.05, power of 0.8 and significance level of 0.05. Based on the above calculation, at last 6 mice were allocated to each experimental group to detect behavioral performance.

MCAO mice in vector injection surgeries were excluded from the analysis if their body weight was less than that of no vector injection surgeries at 8 weeks old. MCAO mice died before the end of the designated study period were excluded from the analysis. Total 10 MCAO mice were excluded from the study.

For other experiments, the numbers per group differed based on the type of assay. We utilized N = 4 for MiRNA sequencing, N = 3–6 depending on the type of biochemical analyses as indicated in each of the figure legends.

Results

Neuronal activity in the M1 was increased following ischemic stroke

At 6 h post-ischemic injury, cerebral blood flow within the ipsilateral hemisphere was significantly reduced in mice subjected to MCAO (Figure S1A). At 24 h post-ischemic injury, MCAO mice displayed typical ischemia phenotypes including neurological deficits (Figure S1B-E), cerebral infarction (Figure S1F), lung injury (Figure S1G) and neuronal apoptosis (Figure S2). The mice of MCAO group suffered more severe ischemia process (2 h of ischemia). The mortality of MCAO group was 30% within 24 h reperfusion, 50% within 3 days reperfusion, 70% within 7 days reperfusion in the groups of MCAO (Figure S3A). Thus, we only observe the effect of inhibiting neuronal activation on brain damage at 2 h of ischemia following 24 h reperfusion.

To observe the long-term outcome of inhibition of neuronal activation, the 1 h occlusion (a milder ischemia) was used to reduce unacceptably high mortality rates. The mortality of MCAO group (1 h of ischemia) was 0 within 24 h reperfusion, 20% within 3 days reperfusion, 40% within 7 days reperfusion in the groups of MCAO (Figure S3A). Notably, MCAO mice displayed cerebral infarction at 24 h after MCAO (1 h of ischemia) (Figure S3B). As expected, the mice with 1 h of ischemia with 24 h, 7 days and 14 days reperfusion exhibited sensorimotor deficits in a battery of behavioral tests after MCAO, including the mNSS, negative geotaxis test, Kondziella's inverted screen test (Figure S3C-E). In contrast, hM4Di + MCAO + CNO mice exhibited a better neurological function at 24 h, 7 days, and 14 days after MCAO (Figure S3F-H).

As peri-infarct depolarizations are closely related with infarct formation and expansion, we first examined neuronal activity via c-Fos expression within the ipsilateral M1 and ischemic core. In response to ischemic stroke, there were significant increases in the expression of c-Fos protein in M1 ($p < 0.01$) and ischemic core ($p < 0.05$) (Figure S4A) as well as in total number of c-Fos$^+$ cells in the M1 ($p < 0.05$) and ischemic core ($p < 0.05$) (Figure S4B). To further explore the identity of the activated neurons after ischemia, we measured the excitatory neuronal marker calcium/calmodulin-dependent protein kinase II α (CaMKIIα) and the inhibitory neuronal marker glutamate decarboxylase 67 (GAD67), which are co-expressed with c-Fos. As shown in Fig. 1A-B, the percentage of c-Fos$^+$ cells in the M1 was significantly increased in the MCAO versus the Sham group ($p < 0.001$) as based on FACS. Importantly, the percentage of CaMKIIα$^+$/c-Fos$^+$ and GAD67$^+$/c-Fos$^+$ neurons in the M1 were significantly increased at 6 h after ischemic stroke ($p < 0.01$, $p < 0.001$, respectively) (Fig. 1A, C), while the percentage of c-Fos$^+$ cells, CaMKIIα$^+$/c-Fos$^+$ and GAD67$^+$/c-Fos$^+$ neurons in M1 were all significantly increased (all $p < 0.01$) at 24 h following MCAO (Figure S5). Consistent with FACS results, the fluorescent staining showed that the number of CaMKIIα$^+$/c-Fos$^+$ ($p < 0.01$) and GAD67$^+$/c-Fos$^+$ neurons ($p < 0.01$) in M1 was increased at 24 h after ischemic stroke (Fig. 1D). These results indicated that ischemic exposure significantly increased the activity of excitatory and inhibitory neurons in the M1.

To further assess the critical role of neuronal-activity in M1 following ischemic stroke, we expressed the human modified muscarinic type 4 DREADDs (hM4Di) or the human modified muscarinic type 3 DREADDs (hM3Dq) receptor in mice at 2 weeks prior to MCAO. These receptors were exclusively activated by designer drugs and were generated via hSyn promoter-driven adeno-associated virus (AAV) infection (Fig. 1E–F). Consistent with the specificity of the hSyn promoter, the presence of the mCitrine$^+$ cell was confirmed in MAP2$^+$ neurons (Fig. 1G) but no co-expression of mCitrine was observed within microglia (Iba-1) (Figure S6). The ability for DREADDs to excite or inhibit neurons was then determined by examining changes in c-Fos expression following clozapine-N-oxide (CNO) administration. Application of CNO increased neuronal activity of M1 compared with Vehicle, which was evidenced by increased proportion of c-Fos$^+$hM3Dq$^+$ neurons in hM3Dq$^+$ neurons ($p < 0.05$)

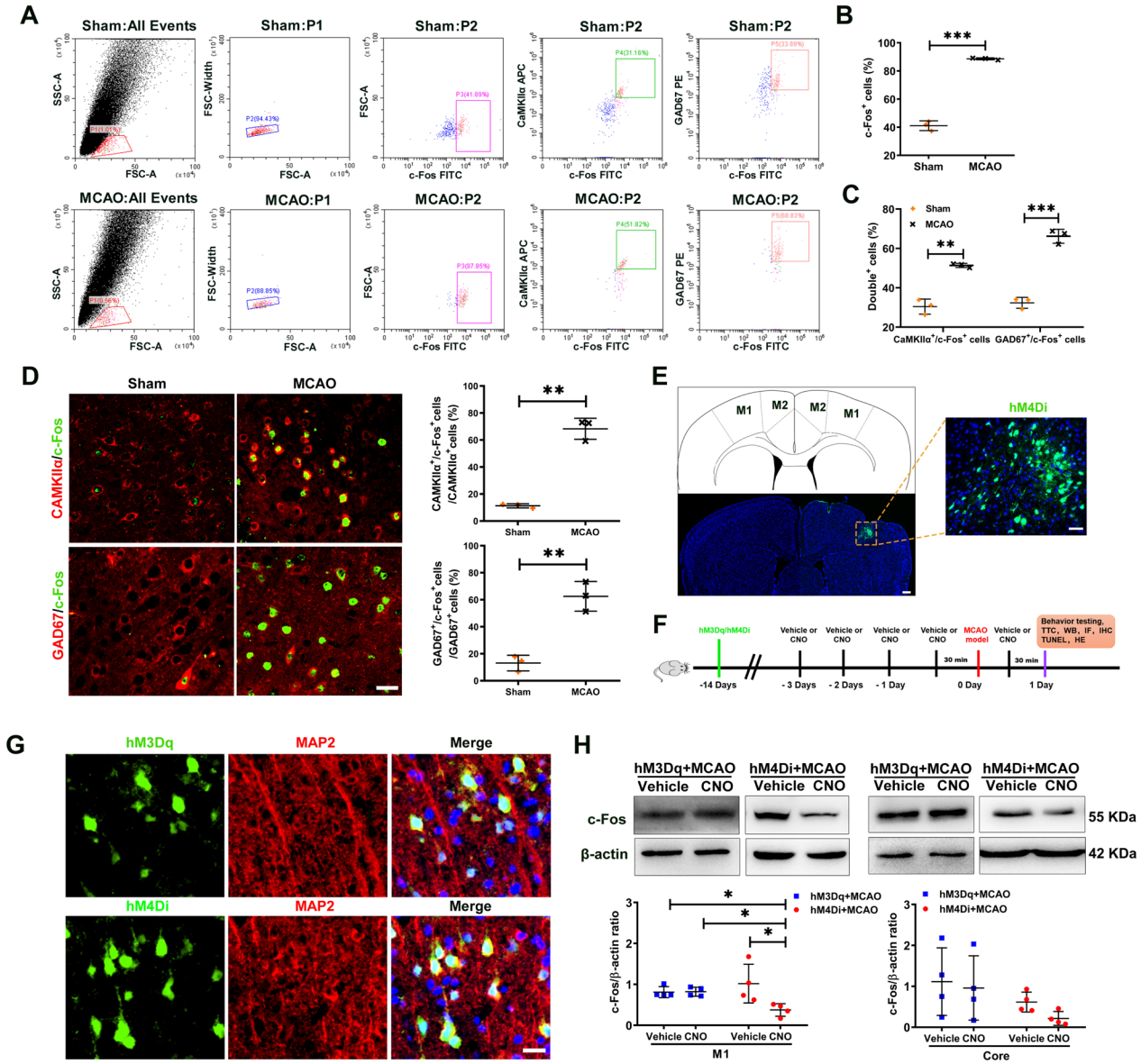

Fig. 1 Chemogenetic inhibition of M1 neuronal activity after ischemic stroke. **A** An example of FACS sorting of c-Fos$^+$ cells, CaMKIIα$^+$/c-Fos$^+$ neurons and GAD67$^+$/c-Fos$^+$ neurons in M1 at 6 h after stroke. Sorting of c-Fos$^+$ cells are located right (P3). Sorting of CaMKIIα$^+$/c-Fos$^+$ neurons (P4) or GAD67$^+$/c-Fos$^+$ neurons (P5) are located in the top right quadrants, respectively. **B** Percentage of c-Fos$^+$ cells by FACS. N = 3/group. **C** Percentage of CaMKIIα$^+$/c-Fos$^+$ neurons and GAD67$^+$/c-Fos$^+$ neurons by FACS. N = 3/group. **D** Representative images and quantification of CaMKIIα$^+$ or GAD67$^+$ cells colabeled with c-Fos$^+$ cells in M1 of Sham and MCAO mice. N = 3/group. Scale bar = 25 μm. **E** Top: Schematic shows location of viral vector (AAV9-hSyn-HA-hM4(Gi)-IRES-mCitrine (hM4Di)) injections (green) in M1. Scale bar = 100 μm. Bottom: Representative imaging shows expression of the mCitrine tag around M1. Scale bar = 50 μm. **F** Experimental design. Two weeks prior to surgery, viral administration was performed under anesthesia. Viral vector contains the DREADDs transgene (hM4Di, AAV9-hSyn-HA-hM3(Dq)-IRES-mCitrine (hM3Dq)). The intraperitoneal (i.p.) injection of clozapine-N-oxide (CNO) (1 mg/kg body weight) or Vehicle was administered in conscious mice for 5 times. CNO or Vehicle (once every 24 h, 3 times in total) was injected intraperitoneally 3 d before MCAO. The fourth injection of CNO or Vehicle was administered at 30 min before MCAO. The last injection of CNO or Vehicle was administered at 23.5 h after MCAO. The chosen doses of CNO did not induce any behavioral signs of seizure activity. At 24 h post-surgery, the tissues were collected for next experiment. **G** hM4Di or hM3Dq (green, infected cell) in M1, co-localize with MAP2 staining (red) 15 d after virus infection. Scale bar = 25 μm. **H** Western blot measurements of c-Fos protein expression in M1 and injury core of hM4Di + MCAO mice or hM3Dq + MCAO mice following Vehicle or CNO treatment at 24 h after stroke. The levels of c-Fos protein were quantitated by normalizing to β-actin. N = 4/group. All data are represented as mean ± SD. ** $p < 0.01$, *** $p < 0.001$ according to *t*-test in B-D. * $p < 0.05$ according to Kruskal–Wallis test in H (in M1). *M1* primary motor cortex, *M2* secondary motor cortex, *TTC* 2,3,5-triphenyltetrazolium chloride monohydrate, *WB* Western blot, *IF* Immunofluorescence staining, *IHC* Immunohistochemistry, *HE* Hematoxylin Eosin

in M1 of Sham mice (Figure S7A). We also found that there was an increase in c-Fos lacking hM3Dq-mCitrine, suggesting that this excitation involved in the local connectivity or circuit network activity. Moreover, CNO treatment decreased c-Fos$^+$hM4Di$^+$ neurons in hM4Di$^+$ neurons ($p < 0.05$) in the M1 of following MCAO (Figure S7B). Importantly, decreasing the activation of M1 neurons with CNO in MCAO mice reduced the number of c-Fos$^+$ cells (Figure S8B) and c-Fos protein levels (Fig. 1H) in the M1 (c-Fos$^+$ cells number: $p < 0.05$; c-Fos protein: $p < 0.05$) and the number of c-Fos$^+$ cells and the c-Fos protein levels in ischemic core showed a downward trend as compared with Vehicle (Figure S8C) (Fig. 1H). However, no changes were observed in the number of c-Fos$^+$ cells and c-Fos protein levels between the hM3Dq + MCAO + CNO and hM3Dq + MCAO + Vehicle group (Fig. 1H, S8). These results indicated that neuronal activation or inactivation was preferentially induced in hM3Dq$^+$ or hM4Di$^+$ neurons in response to CNO administration.

Decreasing M1 neuronal activity rescued neurological impairment and brain infarct area after ischemic stroke in mice

Behavioral performance, including modified neurological severity score (mNSS), negative geotaxis test, Kondziella's inverted screen test and grid-walking test, was measured at 24 h following ischemia. Motor control in all four tasks was impaired in the MCAO group (Figure S1B-E). As shown in Fig. 2A, neurological deficit scores of the hM4Di + MCAO + CNO group were significantly decreased as compared with that of the hM4Di + MCAO + Vehicle group ($p < 0.01$). In the negative geotaxis test, the time required for turning left or right was significantly reduced in the MCAO + hM4Di + CNO compared to the MCAO + hM4Di + Vehicle group ($p < 0.01$) (Fig. 2B). The hM4Di + MCAO + CNO group enhanced limb muscle strength, as indicated by increased latencies to fall off the wire mesh as compared to the hM4Di + MCAO + Vehicle group ($p < 0.001$) (Fig. 2C). There was also a significant reduction in right limb motor performance within the hM4Di + MCAO + CNO versus hM4Di + MCAO + Vehicle group as assessed in the grid-walking test ($p < 0.05$) (Fig. 2D). However, no statistically differences were observed between the hM3Dq + MCAO + CNO and hM3Dq + MCAO + Vehicle group with regard to results obtained in the mNSS, negative geotaxis test, grid-walking test and Kondziella's inverted screen test (Fig. 2A–D). Moreover, decreasing activation of M1 neurons with CNO in MCAO mice reduced the infarct area ($p < 0.001$) (Fig. 2E–F) and apoptosis rate (M1: $p < 0.01$; Core: $p < 0.001$) (Fig. 2G–H), while, no statistically significant differences in infarct area and apoptosis rate were obtained between the hM3Dq + MCAO + CNO and hM3Dq + MCAO + Vehicle group (Fig. 2E–H). Relatively larger infarct area in MCAO mice may have created a ceiling effect (Fig. 2E), thus hM3Dq + CNO did not further increase c-Fos expression, infarct area and apoptosis rate following ischemic stroke.

Moreover, hM4Di or hM3Dq treatments did not alter any potential toxicity to peripheral organs (heart, liver, kidney, spleen and lung) in these studies (Figure S9). It should be noted that hM4Di + CNO treatment improved ischemia-induced lung injury compared with hM4Di + Vehicle. These results suggested that decreasing neuronal activity via CNO/hM4Di significantly suppressed ischemia-induced behavioral impairments and infarct area.

Decreasing M1 neuronal activity inhibited microglia activation and inflammatory responses within the ischemic brain

Immunostaining for Iba-1, a microglia specific marker, was performed to assess the pathological changes of microglia within the ipsilateral hemisphere of MCAO mice. A significant increase in the number of Iba1-positive cells was observed in M1 ($p < 0.001$) (Fig. 3B) and the ischemic core ($p < 0.05$) (Figure S10A) of these mice. Decreasing neuronal activity via CNO/hM4Di treatment in MCAO mice significantly reduced the number of Iba1-positive cells in the M1 ($p < 0.1$) (Fig. 3J) and ischemic core ($p < 0.01$) (Figure S10E) compared to that in the hM4Di + MCAO + Vehicle group. The microglial Sholl analysis was performed to assess the complexity and morphology of microglia. The microglial branching was measured using concentric circles in Sholl analysis. The MCAO mice displayed markedly decreased intersection numbers with the concentric circles in M1 ($p < 0.05$) (Fig. 3D). In contrast, decreasing neuronal activity via CNO/hM4Di treatment in MCAO mice significantly alleviated this decrease in the intersection numbers in the M1 compared to that in the hM4Di + MCAO + Vehicle group ($p < 0.01$) (Fig. 3L). Consistent with these findings, MCAO mice also showed an increase in microglial cell body area ($p < 0.05$) (Fig. 3E) and maximum branch length ($p < 0.05$) (Fig. 3F) in M1. Decreasing neuronal activity via CNO/hM4Di treatment in MCAO mice significantly alleviated the area of the microglia cell body ($p < 0.05$) (Fig. 3M) and increased the maximum branch length ($p < 0.05$) (Fig. 3N) in the M1 compared to that in the hM4Di + MCAO + Vehicle group. In addition, CD68 staining was used to label activated microglia [36]. A significant increase in the number of CD68-positive cells was observed in M1 ($p < 0.05$) (Figure S11A) of these mice. Decreasing neuronal activity via CNO/hM4Di

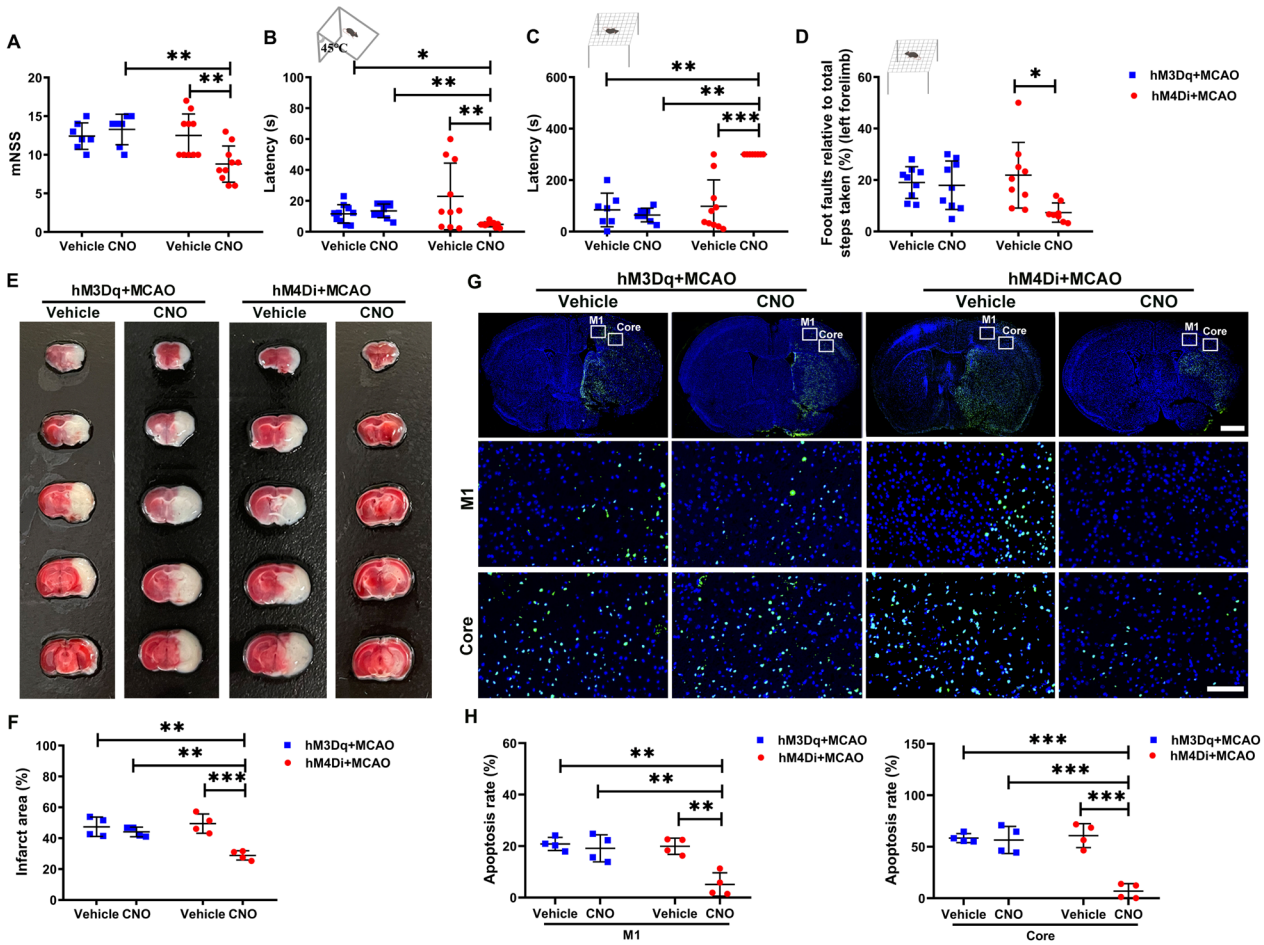

Fig. 2 Decreasing M1 neuronal activity rescued the neurological impairment and brain infarct area after ischemic stroke in mice. Neurological tests, including mNSS **A** (N = 7 for hM3Dq + MCAO + Vehicle group and hM3Dq + MCAO + CNO group, N = 10 for hM4Di + MCAO + Vehicle group and hM4Di + MCAO + CNO group), negative geotaxis test **B** (N = 10/group), Kondziella's inverted screen test **C** (N = 7 for hM3Dq + MCAO + Vehicle group and hM3Dq + MCAO + CNO group; N = 10 for hM4Di + MCAO + Vehicle group and N = 8 for hM4Di + MCAO + CNO group), and grid-walking test **D** (N = 9 for hM3Dq + MCAO + Vehicle group, hM3Dq + MCAO + CNO group, and hM4Di + MCAO + Vehicle group, N = 8 for hM4Di + MCAO + CNO group). **E** Representative TTC staining of brain sections from hM3Dq + MCAO or hM4Di + MCAO mice following Vehicle or CNO treatment, the infarct area is shown in white. **F** Bar graph shows percentages of infarct area of indicated groups. N = 4/group. **G** Top: Representative TUNEL staining of brain sections from mice hM3Dq + MCAO or hM4Di + MCAO mice following Vehicle or CNO treatment. Scale bar = 1 mm. Bottom: Magnification of white frames in M1 and injury core. Scale bar = 100 μm. **H** Bar graph shows percentages of apoptosis rate of indicated groups. N = 4/group. All data are represented as mean ± SD.* $p < 0.05$, ** $p < 0.01$, *** $p < 0.001$ according to Kruskal–Wallis test in **A** –**C**. * $p < 0.05$, ** $p < 0.01$, *** $p < 0.001$ according to two-way ANOVA followed by the Bonferroni's post hoc test in **D**, **F**, **H**

treatment in MCAO mice significantly reduced the number of CD68-positive cells in the M1 ($p < 0.001$) (Figure S11B) compared to that in the hM4Di + MCAO + Vehicle group. Taken together, decreasing neuronal activity via CNO/hM4Di treatment alleviated the over-activation of microglia in the M1 of MCAO mice.

Results from our qRT-PCR assay revealed that mRNA expressions of the pro-inflammatory cytokines, including IL-1β, TNF-α and IL-6 were increased (IL-1β: $p < 0.01$, TNF-α: $p < 0.01$ and IL-6: $p < 0.001$), whereas Arg-1 levels were decreased ($p < 0.01$) (Figure S12A) at 24 h after stroke. Decreasing neuronal activity via CNO/hM4Di in MCAO mice significantly down-regulated IL-1β and IL-6 mRNA levels (all $p < 0.05$), while Arg-1 mRNA levels were upregulated ($p < 0.05$) compared to that obtained in the hM4Di + MCAO + Vehicle group (Figure S12C). Coincident with these cytokine mRNA changes, Western blot assay results showed that a significant increase in protein expression of Iba-1, IL-1β and TNF-α in M1 (all $p < 0.05$) (Fig. 3H) and ischemic core (Iba-1: $p < 0.05$, IL-1β: $p < 0.01$, TNF-α: $p < 0.05$) (Figure S10B) after stroke, whereas Arg-1 levels were decreased in the M1

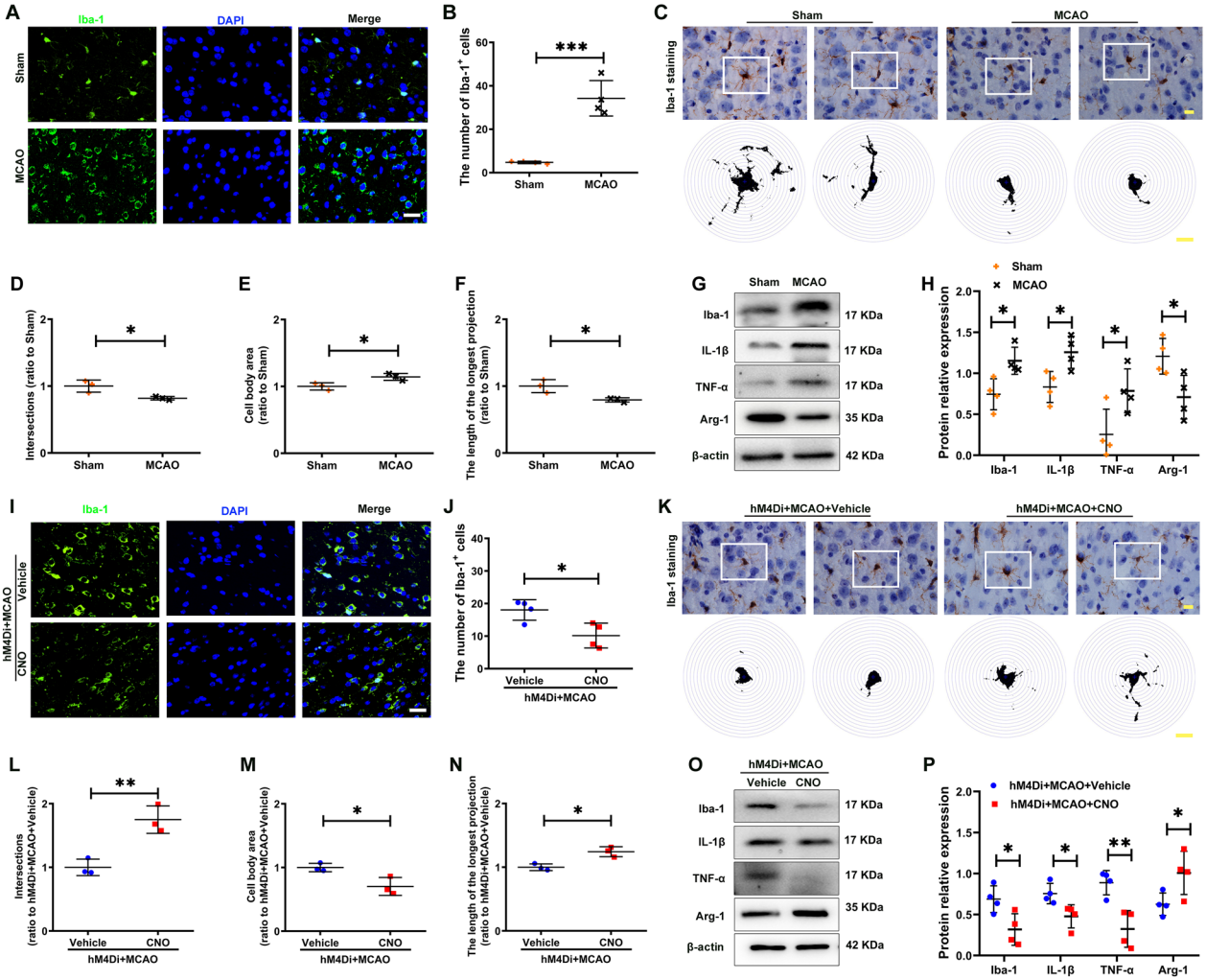

Fig. 3 Decreasing M1 neuronal activity inhibited microglia activation and inflammatory response in M1 of the ischemic brain. **A**, **I** Representative immunofluorescent staining for Iba-1 in the M1 of indicated groups, Scale bar = 25 μm. **B**, **J** Bar graph shows the number of Iba-1$^+$ cell of indicated groups, N = 4/group. **C**, **K** Representative images of Iba1$^+$ microglia and the Sholl analysis, the intersection number per radius over the distance from the cell body was displayed graphically in the curve. Scale bar = 10 μm. **D**–**F**, **L**–**N** The interactions, cell body area and maximum branch length were analyzed. N = 3/group. **G**, **O** Western blot measurements of Iba-1, IL-1β, TNF-α and Arg-1 protein levels in M1 of indicated groups. **H**, **P** The levels of Iba-1, IL-1β, TNF-α and Arg-1 were quantitated by normalizing to β-actin. N = 4/group. All data are represented as mean ± SD. * $p < 0.05$, ** $p < 0.01$, *** $p < 0.001$ according to *t*-test in A, H (IL-1β, TNF-α and Arg-1), **D**–**F**, **J**, **L**–**N** and **P**. * $p < 0.05$ according to Mann–Whitney U test in H (Iba-1)

($p < 0.05$) (Fig. 3H) and ischemic core ($p < 0.05$) (Figure S10B). Importantly, hM4Di-expressing mice treated with CNO showed significantly decreased protein expressions of Iba-1, IL-1β and TNF-α in the M1 (Iba-1: $p < 0.05$, IL-1β: $p < 0.05$, TNF-α: $p < 0.01$) (Fig. 3P) and ischemic core (IL-1β: $p < 0.001$, TNF-α: $p < 0.05$) (Figure S10F), and increased the levels of Arg-1 protein within M1 ($p < 0.05$) (Fig. 3F) and ischemic core ($p < 0.05$) (Figure S10F) versus that of Vehicle controls at 24 h after stroke. However, in these hM3Dq + MCAO mice, administration of CNO had no effect on microglia activation and pro-inflammatory cytokine levels (Figure S10C-D, Figure S12B, Figure S13). These results suggested that decreasing activity via CNO/hM4Di significantly suppressed ischemia-induced neuroinflammation.

Aberrant neuronal activity altered the expression of EVs-miRNA in M1 following ischemia stroke

EVs have been proposed to contribute to neuron-glia communication in various physiological processes of CNS [21, 22]. Accordingly, we first determined whether ischemia-evoked neuronal activity altered the expression of EVs-miRNAs in M1 following MCAO. We collected EVs from M1 at 24 h following ischemic stroke (referred

to as Sham-M1-EVs and MCAO-M1-EVs, respectively) (Fig. 4A). The Sham-M1-EVs and MCAO-M1-EVs were characterized by immunoblotting, TEM, and ZetaView (Fig. 4B–D) as indicated in the MISEV2018 [15]. Both EVs were similar with regard to their protein marker expressions (Fig. 4B), morphology (Fig. 4C) and sizes (Fig. 4D). The quantitative results of the number of EVs in the Sham-M1-EVs group and MCAO-M1-EVs group showed no significant difference (Fig. 4D). The EVs-miRNA contents were analyzed with use of next-generation sequencing. Venn diagrams, as used for determining the number of miRNAs in EVs, revealed that Sham-M1-EVs contained 533 miRNA and MCAO-M1-EVs contains contained 558 miRNA, of which 469 were shared between the two groups (Fig. 4E). Among which 7 were upregulated and 14 downregulated in MCAO-M1-EVs versus Sham-M1-EVs (using at cut-off criteria of $p < 0.01$, Log2 Fold Change > 1) as illustrated in the volcano plot (Fig. 4F) and detailed in the heatmaps (Fig. 4G).

Among the identified M1-EVs miRNA, 365 identified miRNAs (59.1%) overlapped with the EVs miRNA of the Vesiclepedia database (http://microvesicles.org/) (Figure S14A). Moreover, the identified M1-EVs miRNA, 506 identified miRNAs (81.9%) overlapped with the miRNA of primary neuron EVs (neuron-EVs) (SRA No. PRJNA814406) (Figure S14B). The primary neuron was treat with hSyn-hM3Dq + CNO or hSyn-hM3Dq + Vechile in the database (SRA No. PRJNA814406). And 339 miRNAs were detected across all group samples, including miR-100-5p (Figure S14C). Among them, miR-100-5p is the top 35 identified miRNAs in neuron-EVs (SRA No. PRJNA814406) dataset (Figure S14D), and the top 20 identified miRNAs in M1-EVs in this study (Fig. 4H). We found that among which 7 were upregulated (including miR-100-5p, miR-1298-5p, miR-148b-3p, miR-3068-3p, miR-340-5p, miR-9-3p and miR-9b-5p) and 14 downregulated in MCAO-M1-EVs versus Sham-M1-EVs (using at cut-off criteria of $p < 0.01$, Log2 Fold Change > 1) as illustrated in the volcano plot (Fig. 4F) and detailed in the heatmaps (Fig. 4G). More importantly, among the top 7 upregulated miRNAs, the top one differentially expressed miRNA, namely miR-100-5p, was shared between Sham-M1-EVs and MCAO-M1-EVs (Fig. 4H). Following this analysis, miR-100-5p was selected for validation based on their abundance in EVs miRNA cargo in this study.

We further quantified miR-100-5p in M1-EVs or M1 with qRT-PCR and found that miR-100-5p was significantly upregulated in both M1-EVs ($p < 0.01$) and M1 ($p < 0.05$) of MCAO mice (Fig. 4I). Pearson correlation analysis was performed to assess any possible relationships among miR-100-5p levels within M1-EVs or M1 and stroke severity. There was a significant correlation between miR-100-5p level of M1-EVs or M1 and infarct area (Figure S15A-B). In contrast, miR-100-3p was detected at much lower levels in both EVs, and no significant difference was present between EVs in these two groups (Figure S15C-D).

Next, we examined whether ischemia-evoked neuronal activity would change miR-100-5p expression in neurons as assessed in vitro. To establish an ischemic model in vitro, PC12 cells were exposed to OGD/R, with our initial study addressing the issue of whether OGD/R exposure would evoke neuron activation. As c-Fos expression is rapidly and transiently induced by neuronal activity in response to an elevation in intracellular

(See figure on next page.)

Fig. 4 Neuronal activity altered the expression of EVs-miRNA in M1 following ischemia stroke. **A** Schematic of the EVs isolation method from the M1 of Sham and MCAO mice (referred to as Sham-M1-EVs and MCAO-M1-EVs). **B** Western blot analysis of brain lysate and associated EVs (Sham-M1-EVs and MCAO-M1-EVs) for identified specific EVs proteins, as well as common EVs (CD9, CD63) and non-EVs (calnexin) protein markers. **C** Transmission electron microscopy (TEM) images of isolated Sham-M1-EVs and MCAO-M1-EVs. Scale bar = 50 nm. **D** Size distribution of the isolated Sham-M1-EVs and MCAO-M1-EVs determined using ZetaView. The quantity of Sham-M1-EVs group and MCAO-M1-EVs group were measured using ZetaView. N = 3/group. **E** EVs miRNA abundance analysis by next-generation sequencing. Venn diagrams of the number of miRNA in M1-derived EVs from Sham mice (referred to as Sham-M1-EVs) and MCAO mice (referred to as MCAO-M1-EVs). The number in the center refers to miRNAs with no specific expression in M1-EVs studied. **F** Volcano plot of differential miRNA expression. The black dots represent the miRNA with no significant difference, the red dots represent the significantly upregulated differential miRNA, and the green dots represent the significantly downregulated differential miRNA. Black arrow indicates miR-100-5p. **G** Heatmap displaying of differential miRNA expression. MiRNA expression is hierarchically clustered on the y-axis, and M1-EVs from Sham and MCAO mice are hierarchically clustered on the x-axis. High expression based on normalized Ct is shown in red and low expression in blue. **H** The top 20 abundant miRNA in Sham-M1-EVs and MCAO-M1-EVs are shown. **I** qRT-PCR measurements of miR-100-5p in Sham-M1-EVs and MCAO-M1-EVs (N = 3 pools within Sham-M1-EVs group, and MCAO-M1-EVs group, 4 brains per pool), and M1 of Sham and MCAO mice (N = 4/group). **J** qRT-PCR measurements of miR-100-5p in Nor-N-EVs and OGD-N-EVs (N = 3/group), and normal and OGD/R-exposed PC12 cells (N = 6 for Normal group and N = 5 for OGD/R group). **K** Primary neuron, microglia and astrocytes were exposed to OGD/R, the expression of miR-100-5p in cells were detected by qRT-PCR. N = 5 for Control group in primary neuron and N = 6 for others group. **L** PC12 cells, BV-2 cells and fetal-derived normal human astrocytes (NHA) were exposed to OGD/R, the expression of miR-100-5p in cells were detected by qRT-PCR. N = 6/group. **M** BV-2 cells were incubated with OGD-N-EVs or OGD-N-EVs for 24 h, the expression of miR-100-5p in cells were detected by qRT-PCR. N = 4/group. All data are represented as mean ± SD. * $p < 0.05$, ** $p < 0.01$, *** $p < 0.001$ according to *t*-test in I (left), J, K (primary neuron) and L. * $p < 0.05$ according to Mann-Whitney U test in I (right) and M.

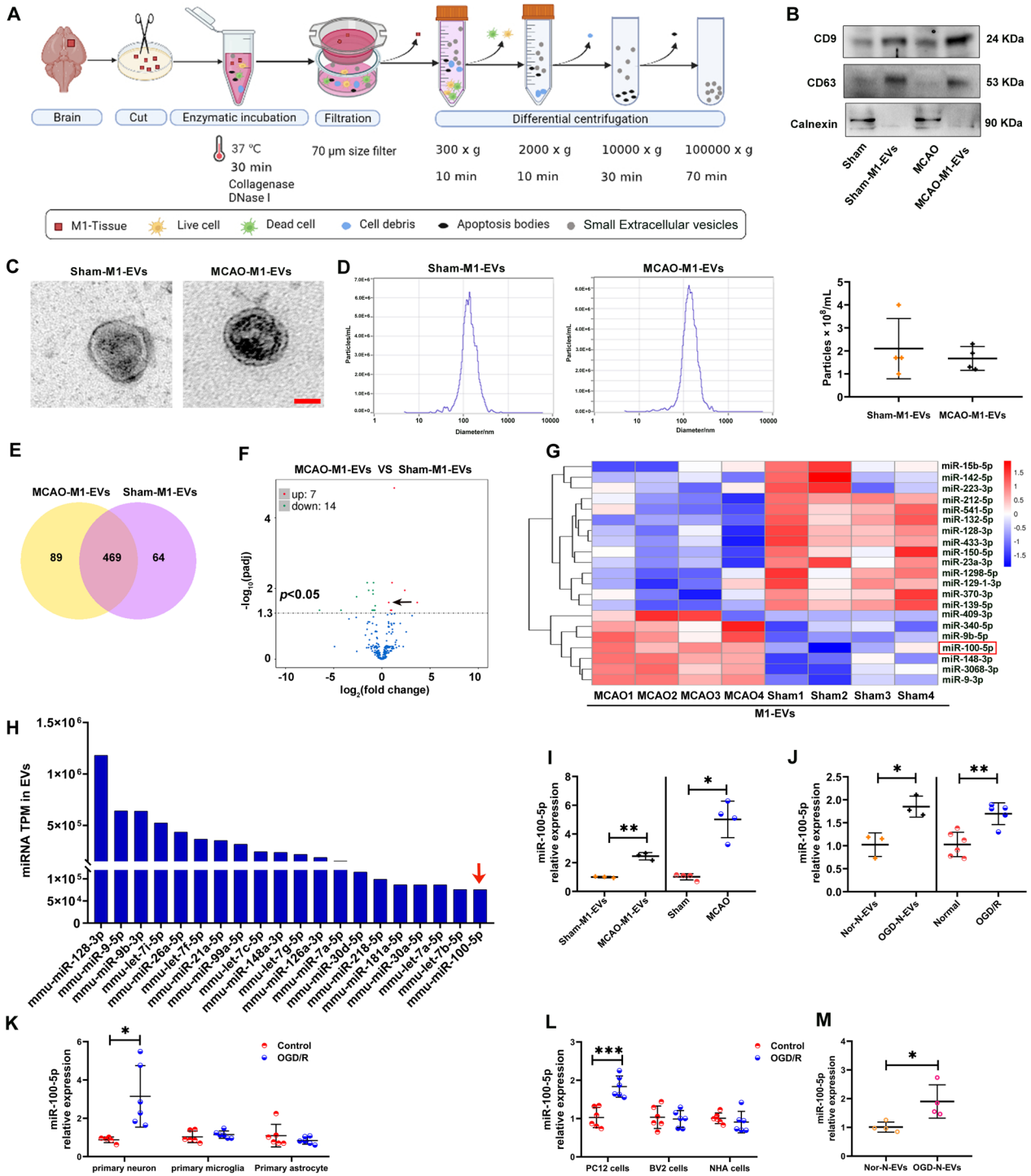

Fig. 4 (See legend on previous page.)

Ca^{2+} concentration, intracellular Ca^{2+} concentrations and c-Fos expression were measured as a means to assess neuron activation following OGD/R exposure. In a preliminary experiment, we found that a 6 h OGD exposure with reoxygenation for 3 or 12 h significantly increased c-Fos mRNA expression (all $p < 0.05$) in these cells (Figure S16A-B). In order to collect adequate levels of EVs from PC12 cells, we used a 6 h exposure of OGD and reoxygenation for 12 h (referred to as OGD/R) to simulate an ischemic-induced activation state of neurons in

subsequent experiments. We found that this OGD/R model resulted in increased levels of intracellular Ca^{2+} ($p < 0.05$) as well as c-Fos protein expression ($p < 0.05$) (Figure S16C-E) and neuronal apoptosis ($p < 0.001$) (Figure S16F) in these PC12 cells. Importantly, OGD for 6 h and reoxygenation for 12 h remarkably increased miR-100-5p expression in the cellular compartment of PC12 cells ($p < 0.05$) (Figure S17). Moreover, OGD/R-exposed neuron also increased miR-100-5p in EVs ($p < 0.05$), in addition to increasing cellular miR-100-5p in PC12 cells ($p < 0.01$) (Fig. 4J, S17B).

We next assessed whether the source of miR-100-5p resided in neurons versus glia cells. The expression of miR-100-5p in glial cells was not affected by OGD/R stress, but the expression of miR-100-5p in neurons significantly increased after OGD/R stress (Fig. 4K–L), suggesting that neurons might be the local source for miR-100-5p in response to ischemia stroke. To test this hypothesis, purified EVs from normal neurons (referred to as Nor-N-EVs) and OGD/R-exposed neurons (referred to as OGD-N-EVs) were collected. BV-2 cells were then treated in vitro with OGD-N-EVs (which contained far greater levels of miR-100-5p levels than Nor-N-EVs), resulting in increased miR-100-5p levels in BV-2 cells ($p < 0.05$) (Fig. 4M). We speculated that with ischemia insult there would be an up-regulated of neuronal miR-100-5p expression, leading to increased loading of miR-100-5p into EVs. Based on a previous report, miR-100-5p was identified as a potent TLR7 activator and inducer of neuroinflammatory and neurodegenerative effects in LPS treated mice [37]. Here, we focused on the role of EVs-miR-100-5p upon neuronal activity within the M1 and the accompanying neurotoxicity following ischemia stroke.

Aberrant neuronal activity-releasing EVs led to microglia activation and neuron apoptosis in vitro

EVs are released from within cultured neurons in an activity-dependent manner [26] and can be internalized within microglia and suppress LPS-induced microglia activation [25]. Therefore, we next directed our attention to determine whether EVs from ischemia-evoked neuronal activity can contribute to neuron-microglia intercellular communication. The Nor-N-EVs and OGD-N-EVs were characterized by TEM, ZetaView and immunoblotting (Fig. 5A–C), which confirmed that the isolated particles were indeed EVs. Moreover, the quantitative results of the number of EVs in the Nor-N-EVs group and OGD-N-EVs group showed no significant difference (Fig. 5B). To verify the delivery of EVs to neuron or microglia, the plasmid encoding a CD63 EVs marker was transfected into PC12 cells (Fig. 5D, S18A), and then collected Nor-N-EVs and OGD-N-EVs (referred to as CD63-labeled Nor-N-EVs and CD63-labeled OGD-N-EVs, respectively). The CD63-labeled EVs could accumulate in BV-2 and PC12 cells at 24 h following treatment (Fig. 5D). PKH67-labeled OGD-N-EVs also accumulated in primary microglia and primary neurons, as well as in BV-2 and PC12 cells at 24 h following treatment (Fig. 5E). After incubating neurons and microglia with PKH67-only, few green fluorescence was observed in PC12 cells and BV-2 cells (Figure S19). Next, we aimed to determine whether N-EVs could render neuro-inflammation, BV-2 cells or primary microglia were pre-incubated with Nor-N-EVs (2×10^{11} particles/mL, 50 μg) or OGD-N-EVs (2×10^{11} particles/mL, 50 μg) for 24 h and then protein was extracted (Figure S18D). Results showed that OGD-N-EVs treatment increased levels of IL-1β protein (all $p < 0.05$), while levels of Arg-1 protein were decreased (all $p < 0.05$) in BV-2 cells and primary microglia as compared with that of Nor-N-EVs treatment (Fig. 5F–H). In contrast, Nor-N-EVs treatment did not affect IL-1β and Arg-1 protein levels in primary microglia (Fig. 5F, G) or BV-2 cells (Fig. 5F, H). In order to further verify the role of EVs, we used GW4869 to inhibit the secretion of EVs in PC12 cells. The results showed that the effect of OGD-N-EVs on BV2 cells was reversed by GW4869 (IL-1β: $p < 0.05$,Arg-1: $p < 0.05$) (Figure S20C-D). Accordingly, Nor-N-EVs and OGD-N-EVs exerted similar effects within BV-2 cells and primary microglia. As the transfection efficiency of primary microglia cells was relatively low, BV-2 cells were used in subsequent experiments. Doses of neuron-derived EVs (N-EVs) including 4×10^{10} particles/mL (10 μg), 2×10^{11} particles/mL (50 μg) and 4×10^{11} particles/mL (100 μg) were selected based on data from our pilot study. The 2×10^{11} particles/mL (50 μg) OGD-N-EVs produced the maximal proinflammatory effect in microglia (Figure S20A-B).

PC12 cells were pre-incubated with Nor-N-EVs or OGD-N-EVs (50 μg/mL) for 24 h and then exposed or not to OGD/R to assess effects upon cell viability. Compared with Nor-N-EVs, OGD-N-EVs treatment induced cell apoptosis not only in normal PC12 cells ($p < 0.001$), but also in OGD/R-exposed PC12 cells ($p < 0.001$) (Figure S21). Collectively, these data indicated that EVs released by ischemia-evoked neuronal activity modulated microglia activation and neuronal viability via autocrine or paracrine mechanisms.

EVs-miR-100-5p secreted by ischemic neurons activate neurons and subsequent neuronal apoptosis

As noted above, the increased neuronal activity of neuron was associated with miR-100-5p expression in neuron and neuron-derived EVs (Fig. 4J). Given these findings, we next investigated whether an up-regulation of miR-100-5p was similarly activity dependent. The

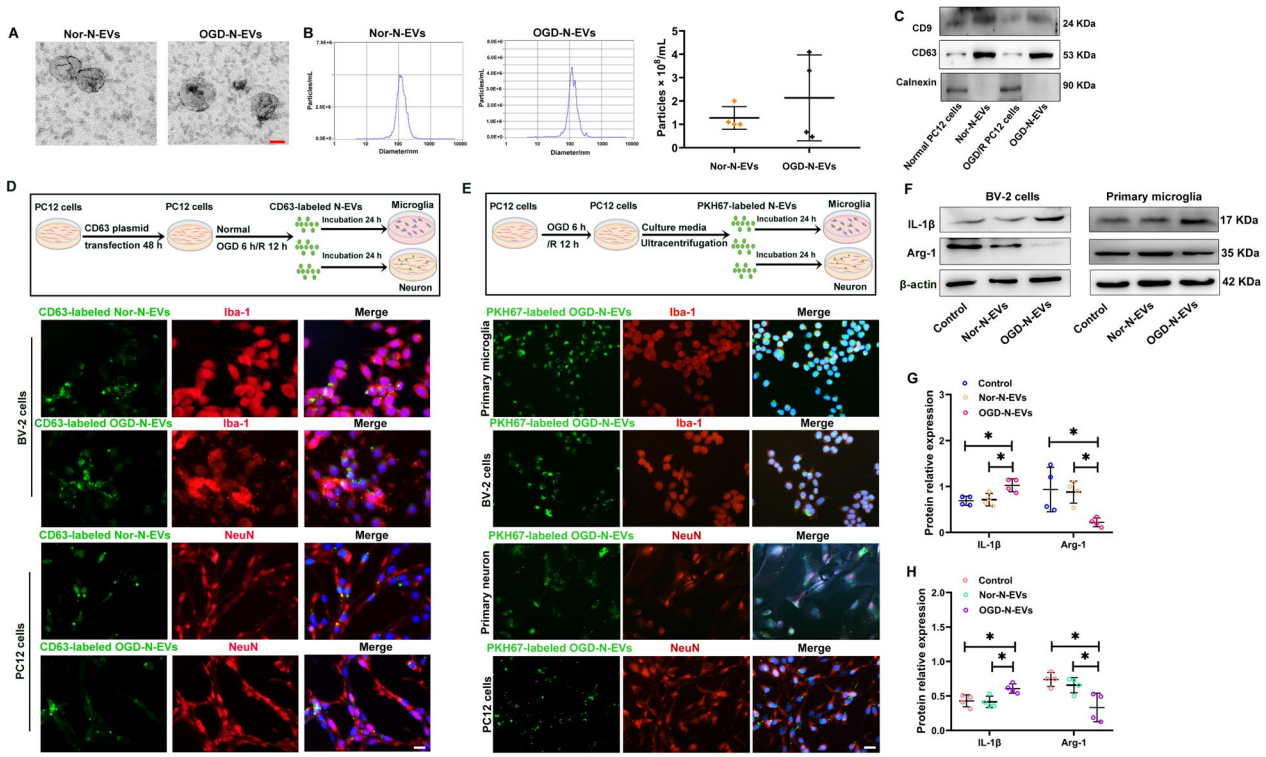

Fig. 5 Neuronal activity-releasing EVs led to microglia activation in vitro. **A** TEM images of EVs from normal PC12 cells (referred to as Nor-N-EVs) and OGD/R-exposed PC12 cells (referred to as OGD-N-EVs). Scale bar = 50 nm. **B** The Size distribution and quantity of the isolated Nor-N-EVs and OGD-N-EVs were determined using ZetaView. N = 3/group. **C** Western blot analysis of Nor-N-EVs and OGD-N-EVs for identified specific EVs proteins, as well as common EVs (CD9, CD63) and non-EVs (Calnexin) protein markers. **D** Top: An in vitro experiment illustration for CD63 labeled EVs. Bottom: CD63 plasmid was transfected with PC12 cells for 48 h and then exposed OGD/R or not, finally collected EVs (referred to as CD63-labeled OGD-N-EVs and CD63-labeled Nor-N-EVs). The collected EVs incubated with BV-2 cells or PC12 cells for 24 h. Then staining with Iba-1 (red) or NeuN (red) and DAPI (blue). Scale bar = 20 μm. **E** Top: An in vitro experiment illustration for PKH67-labeled OGD-N-EVs. Bottom: PKH67-labeled OGD-N-EVs were engulfed by Iba-1 labeled primary microglia and BV-2 cells at 24 h following EVs treatment. PKH67-labeled OGD-N-EVs were engulfed by NeuN labeled primary neuron and PC12 cells at 24 h following EVs treatment. Scale bar = 50 μm. **F** Western blot measurements of IL-1β and Arg-1 protein of BV-2 cells and primary microglia 24 h following Nor-N-EVs and OGD-N-EVs treatment. **G** The levels of IL-1β and Arg-1 of BV-2 cells were quantitated by normalizing to β-actin. N = 4/group. **H** The levels of IL-1β and Arg-1 of primary microglia were quantitated by normalizing to β-actin. N = 4/group. All data are represented as mean ± SD. * $p < 0.05$ according to one-way ANOVA followed by Bonferroni's post hoc test

neuronal activity was stimulated via hM3Dq or hM4Di plasmid transfection. Results from microscopy imaging demonstrated the expected localization of expressed hM3Dq or hM4Di plasmid within plasma membranes of transfected cells (Fig. 6A, S22A). Whole-cell recording of hM3Dq-transfected primary neurons indicated that the addition of CNO (10 μM) remarkably increased the firing frequency of action potentials (Fig. 6B). By contrast, 10 μM of CNO remarkably decreased the firing frequency in hM4Di-plasmid transfected primary neurons (Figure S22B), results which substantiated the effective transfection efficacy of plasmid. Subsequently, intracellular changes in Ca^{2+} and increased c-Fos expression were observed in hM3Dq plasmid transfected neurons after CNO treatment. The Ca^{2+} fluorescent signal intensity and c-Fos expression within hM3Dq-plasmid-transfected neurons were remarkably enhanced after CNO treatment compared with that observed in Vehicle controls ($p < 0.05$, $p < 0.05$, respectively) (Fig. 6C–E). In addition, following CNO treatment, hM3Dq-plasmid-transfected neurons exhibited increased levels of miR-100-5p expression in PC12 cells ($p < 0.05$) (Fig. 6F).

PC12 cells were transiently transfected with FAM (green)-tagged miR-100-5p and EVs were collected (referred as miR-100-5p-EVs) to culture with primary neurons and PC12 cells. MiR-100-5p-EVs (2×10^{11} particles/mL, 50 μg) was then detected in these primary neurons and PC12 cells (Figure S23A). PC12 cells were then pre-incubated with Nor-N-EVs (2×10^{11} particles/mL, 50 μg) or OGD-N-EVs (2×10^{11} particles/mL, 50 μg) for 24 h and miR-100-5p levels were assessed. We found that increased levels of miR-100-5p expression were observed in PC12 cells incubated with OGD-N-EVs, which were substantially greater than that in PC12 cells incubated

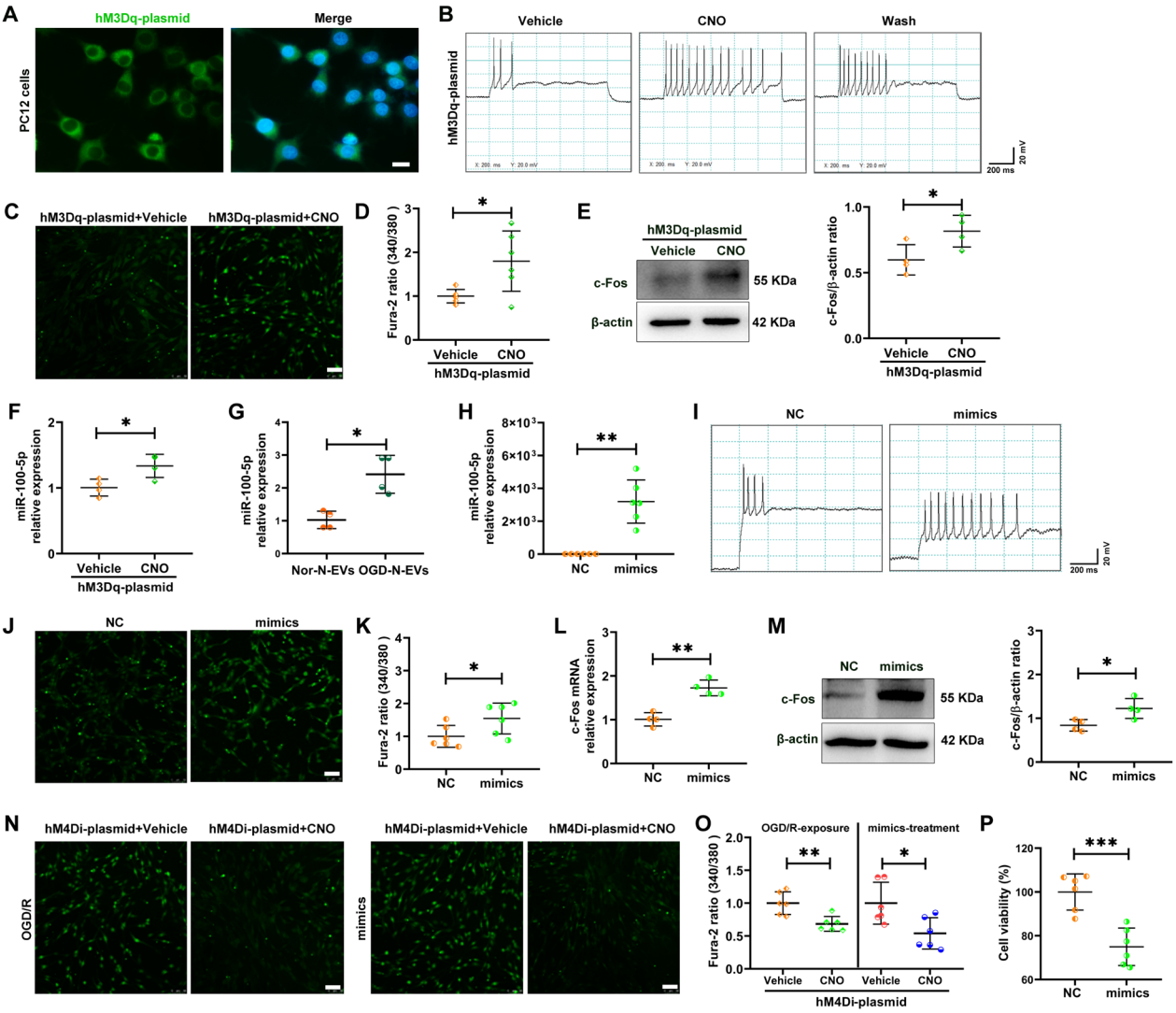

Fig. 6 MiR-100-5p showed positive feedback of neuronal activity. **A** PC12 cells were transfected with hM3Dq plasmid for 48 h, then fixed and taken the images. Scale bar = 20 μm. **B** Primary neuron were transfected with the hM3Dq plasmid for 48 h, then 10 μM CNO was added to cell cultures, and the firing of action currents in primary neurons was recorded. **C** After PC12 cells were transfected with hM3Dq plasmid for 48 h, 3 μM CNO or the Vehicle control was added to detect calcium imaging by confocal microscopy. Scale bar = 50 μm. **D** After PC12 cells were transfected with hM3Dq plasmid for 48 h, 3 μM CNO or the Vehicle control was added to detect the intracellular Ca^{2+} changes by microplate reader. N = 6/group. **E** The level of c-Fos was measured 48 h following hM3Dq plasmid transfection with western blot. The levels of c-Fos were quantitated by normalizing to β-actin. N = 4/group. **F** The level of miR-100-5p in cells from hM3Dq plasmid transfection with PC12 cells. N = 4/group. **G** PC12 cells were incubated with OGD-N-EVs or OGD-N-EVs for 24 h, the expression of miR-100-5p in PC12 cells were detected by qRT-PCR. N = 4/group. **H** The level of miR-100-5p in cells from miR-100-5p mimics (mimics) treatment with PC12 cells. **I** Primary neuron was transfected with the mimics or NC for 48 h, and the firing of action currents in primary neurons was recorded. N = 6/group. **J** After PC12 cells were transfected with miR-100-5p mimics (mimics) for 48 h, calcium imaging was detected by confocal microscopy. Scale bar = 50 μm. **K** Ca^{2+} concentrations in PC12 cells were measured 48 h following miR-100-5p mimics (mimics) treatment with a microplate reader. N = 6/group. **L** The level of c-Fos mRNA was measured at 24 h following miR-100-5p mimics (mimics) treatment by qRT-PCR. N = 4/group. **M** The level of c-Fos was measured 48 h following miR-100-5p mimics (mimics) treatment with western blot. The levels of c-Fos were quantitated by normalizing to β-actin. N = 4/group. **N** After PC12 cells were transfected with hM4Di plasmid with/without OGD/R-exposure or miR-100-5p mimics (mimics) treatment, and then the calcium imaging was detected by confocal microscopy. Scale bar = 50 μm. **O** PC12 cells were transfected with hM4Di plasmid with/without OGD/R-exposure or miR-100-5p mimics (mimics) treatment, and then measured Ca^{2+} concentrations by a microplate reader. N = 6/group. **P** CCK8 measurements of PC12 cell viability following 50 nM of miR-100-5p mimics (mimics) and its negative control (NC) treatment. N = 6/group. All data are represented as mean ± SD. * $p < 0.05$, ** $p < 0.01$, *** $p < 0.001$ according to *t*-test

with Nor-N-EVs (Fig. 6G). The presence of miR-100-5p within the lumen was investigated by RT-PCR. Nor-N-EVs and OGD-N-EVs were digested with proteinase K alone, or following by RNase A digestion [30]. These treatments did not abolish the detection of miR-100-5p in EVs. In contrast, treatment of EVs preparations with detergent to lyse membrane vesicles (Triton-X-100) and RNase A digestion effectively abolished miR-100-5p presence in both EVs (Figure S23B), which indicated that extracellular miR-100-5p was primarily encased within a membrane rather than being directly released.

To assess the effect of miR-100-5p on neuronal activity, we transfected miR-100-5p mimics into PC12 cells (Fig. 6H). With this procedure, we found that miR-100-5p overexpression increased the firing frequency of action potentials (Fig. 6I), Ca2+ levels ($p<0.05$) (Fig. 6J–K), c-Fos mRNA and protein expression ($p<0.01$, $p<0.05$, respectively) (Fig. 6L–M) in these PC12 cells. To further evaluate the effect of OGD/R exposure or extracellular miR-100-5p on neuronal activity, transfection of the hM4Di plasmid following OGD/R exposure or miR-100-5p mimics-treatment upon neurons were determined in vitro. The hM4Di-plasmid + CNO treatment suppressed the increases in Ca^{2+} levels resulting from OGD/R exposure ($p<0.01$) or miR-100-5p mimics treatment ($p<0.05$) in PC12 versus that observed in Vehicle control treatment (Fig. 6N–O). Exposure to miR-100-5p mimics led to a similar reduction in neuronal viability (Fig. 6P). These results provided evidence that increased neuronal activity promoted up-regulation of miR-100-5p in neurons and neuron-secreted EVs, while the transfer of miR-100-5p via EVs to local neurons promoted neuronal activity and subsequent apoptosis.

EVs-MiR-100-5p activated innate immune responses and neurotoxicity via its $U_{18}U_{19}G_{20}$-containing motif and direct association with TLR7

To further substantiate that the biological activity of EVs-contain miR-100-5p from neurons via a paracrine mediator of neuron-microglia intercellular communication, culture media was collected from PC12 cells at 24 h after transfection with miR-100-5p-mimics (referred as miR-100-5p-EVs) or its negative control (referred as NC-EVs). As shown in Fig. 7A, fluorescently labeled miR-100-5p-EVs (2×10^{11} particles/mL, 50 μg) was detected in primary microglia and BV-2 cells following this 24 h incubation period. MiR-100-5p-EVs led to increased expressions of IL-1β ($p<0.01$) and TNF-α ($p<0.05$), while decreased Arg-1 ($p<0.05$) expression was observed as compared to NC-EVs treated BV-2 cells (Fig. 7B). The miR-100-5p mimics or its NC were then used to treat BV-2 cells, with the result that these miR-100-5p mimics led to an increased expression of IL-1β ($p<0.05$) and TNF-α ($p<0.05$), while decreased Arg-1 ($p<0.01$) expression (Fig. 7C) in BV-2 cells. The results of these experiments suggested that regulation of inflammatory responses in microglia were mediated by the transfer of miR-100-5p as derived from neuron-EVs following ischemia insult.

Interestingly, miR-100-5p contains GU-rich sequence motifs of at least 4-nucleotides in length (shown within the shaded region in Fig. 7D), which has been previously described to be capable of inducing TLR7 signaling in mouse microglia and human-derived macrophages [37]. We found that both extracellular miR-100-5p (Figure S24) and miR-100-5p-EVs were co-localized with TLR7 in microglia (Figure S25A) and that TLR7 was localized to endosomes of microglia (Figure S25B). In contrast, miR-100-5p-EVs and miR-100-5p mimics did not affect TLR7 expression levels in BV-2 cells (Fig. 7B and C).

TLR7, as expressed in murine microglia, can be activated by the sequence motif UUGU [38]. Accordingly, we then investigated the relative importance of each U or G in the miR-100-5p seed sequence and the necessity of the $U_{18}U_{19}G_{20}U_{21}$ motif for miR-100-5p-induced IL-1β production, as achieved by individually mutating each U or G (shown in red markers in Fig. 7D). Our results revealed that $G_6\rightarrow A$ or $U_7\rightarrow A$ mutation in the seed sequence did not affect the expression of IL-1β (Fig. 7E). Moreover, either $U_{18}\rightarrow A$ or $U_{19}\rightarrow A$ or $G_{20}\rightarrow A$, but not $U_{21}\rightarrow A$, all within the motif, abrogated IL-1β production (Fig. 7D–E). As expected, all "U" and "G" mutations to "A" in the seed sequence and motif of miR-100-5p abolished the role of miR-100-5p. These data suggested that the consecutive U_{18}, U_{19} and G_{20} within $U_{18}U_{19}G_{20}U_{21}$ motifs were absolutely essential for the ability of miR-100-5p to activate IL-1β production. These findings were consistent with a recent report that the consecutive UU was important for synthetic small ssRNA binding to and activation of the crystal structure of TLR7 [39].

To demonstrate whether miR-100-5p exerted its effects through a physical interaction with TLR7. HEK293T cells were transfected with the miR-100-5p/miR-100-5p mut $G_6G_{20}U_7U_{18}U_{19}U_{21}\rightarrow$ AAAAAA and TLR7 plasmid. TLR7 was immunoprecipitated using a specific anti-TLR7 antibody (Fig. 7F) and western blot of TLR7 (Fig. 7G) showed an effective pulldown of TLR7 by anti-TLR7, but not by anti-IgG. Subsequent qRT-PCR analysis of the TLR7 immunoprecipitates showed that miR-100-5p was enriched in the immunoprecipitates of TLR7 + miR-100-5p transfected cells but not in that of TLR7 + mut $G_6G_{20}U_7U_{18}U_{19}U_{21}\rightarrow$ AAAAAA transfected cells (Fig. 7H). Overexpression of TLR7 with a plasmid transfection further aggravated miR-100-5p-induced IL-1β expression in HEK293T cells ($p<0.01$) (Fig. 7I). In contrast, a down regulation

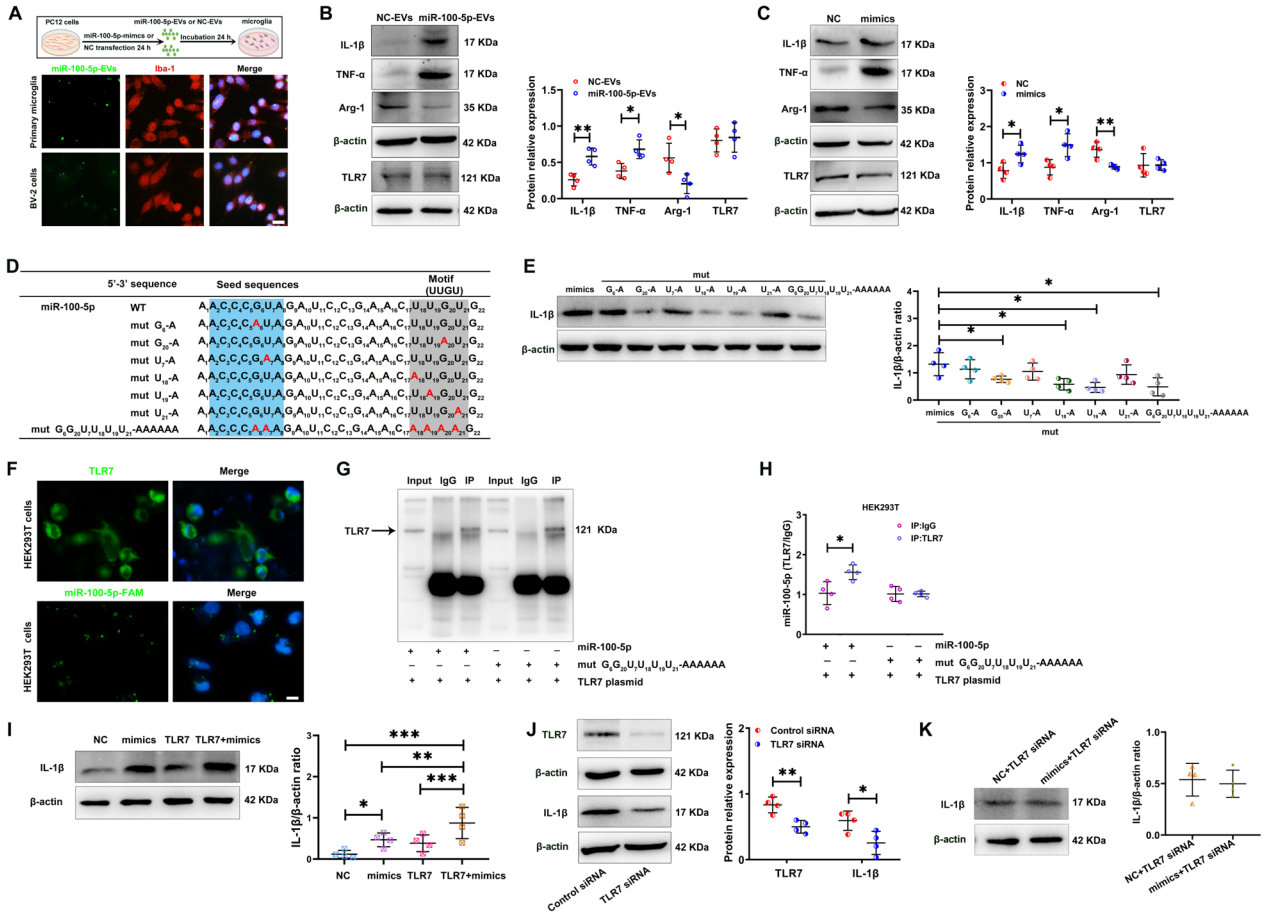

Fig. 7 MiR-100-5p activated innate immune response and neurotoxicity via its $U_{18}U_{19}G_{20}$-containing motif and direct association with TLR7. **A** Top: Experimental design, PC12 cells were transfected with 50 nM NC or miR-100-5p mimics for 24 h, and collected EVs (referred as NC-EVs and miR-100-5p-EVs). Bottom: Primary microglia and BV-2 cells were incubated with miR-100-5p-EVs (5-Carboxyfluorescein, FAM) (green) for 24 h. Cells were then fixed and stained with Iba-1 (red). Scale bar = 25 μm. **B** Western blot measurements of IL-1β, TNF-α, Arg-1 and TLR7 protein of BV-2 cells following NC-EVsand miR-100-5p-EVs treatment for 24 h. N = 4/group. **C** Western blot measurements of IL-1β, TNF-α, Arg-1 and TLR7 protein of BV-2 cells following 50 nM miR-100-5p mimics (mimics) and its negative control (NC) treatment for 48 h. The levels of IL-1β, TNF-α, Arg-1 and TLR7 were quantitated by normalizing to β-actin. N = 4/group. **D** Nucleotide sequences of miR-100-5p and its various U/A and or G/A mutants. The $U_{18}U_{19}G_{20}U_{21}$ motif sequence is highlighted in gray shade. The seed sequences are highlighted in blue shade. U/A and or G/A mutants are in red. **E** Western blot measurements of IL-1β protein of BV-2 cells following 50 nM of miR-100-5p or its various U/A and or G/A mutants treatment. N = 4/group. **F** HEK293T cells were transfected with TLR7 plasmid (green) and with/without miR-100-5p-FAM (green). Scale bar = 20 μm. **G** Representative immunoprecipitation (IP) using anti-IgG or anti-TLR7 antibody in HEK293T cells followed by western blot for TLR7. **H** qRT-PCR analysis of miR-100-5p associated with TLR7. N = 4/group. **I** Western blot measurements of IL-1β of HEK293T cells following 50 nM of miR-100-5p mimics (mimics) with/without TLR7 plasmid (2 μg/mL) transfection. The levels of IL-1β were quantitated by normalizing to β-actin. N = 4/group. **J** Expression of TLR7 in BV-2 cells was knocked down via siRNA technology. TLR7 and IL-1β protein was measured with western blot. The levels of TLR7 and IL-1β were quantitated by normalizing to β-actin. N = 4/group. **K** BV-2 cells were transfected with TLR7 siRNA (50 nM) and miR-100-5p mimics (mimics) (50 nM) or its negative control (NC) for 48 h. The levels of IL-1β were investigated by western blot. The levels of IL-1β were quantitated by normalizing to β-actin. N = 4/group. All data are represented as mean ± SD. * $p < 0.05$, ** $p < 0.01$ according to *t*-test in B, C, E, H, J and K. * $p < 0.05$, ** $p < 0.01$, *** $p < 0.001$ according to one-way ANOVA followed by Bonferroni's post hoc test in I

of TLR7 expression with siRNA suppressed IL-1β expression in BV-2 cells microglia ($p < 0.05$) (Fig. 7J), which could not be reversed with miR-100-5p mimics treatment ($p > 0.05$) (Fig. 7K). Together, these data suggested that miR-100-5p up-regulated pro-inflammatory cytokine production by directly binding and activating TLR7.

Next, we examined whether extracellular miR-100-5p or miR-100-5p-EVs entered neurons and localized to TLR7. Extracellular miR-100-5p (Figure S26) or miR-100-5p-EVs (Figure S27A) entered cells within 24 h of exposure and co-localized to TLR7 in primary neurons and PC12 cells. Consistent with results from previous studies [40], we found that TLR7

was localized to the endosomes of neurons (Figure S27B). Exposure to miR-100-5p mimics led to a similar reduction in neuronal viability (Fig. 6L), however, as compared with the mimics group, neuronal viability of the mut $G_6G_{20}U_7U_{18}U_{19}U_{21} \rightarrow$ AAAAAA (mut) group was significantly increased (Figure S28A). A down regulation in the expression TLR7 with siRNA increased neuronal viability ($p < 0.05$), which could not be reversed by miR-100-5p mimics treatment ($p > 0.05$) (Figure S28B-D). Taken together, these findings indicated that via EVs, miR-100-5p could enter microglia or neurons and located with TLR7. In addition, extracellular miR-100-5p stimulated cytokine production and neurotoxicity by binding and activating TLR7 via its $U_{18}U_{19}G_{20}$-containing motif.

MiR-100-5p activated NF-κB by TLR7 signaling in microglia and neuron

TLR7 ligations induce signal transduction which activate nuclear factor kappa beta (NF-kB) to result in the production of proinflammatory cytokine and chemokines [41]. The issue of whether extracellular miR-100-5p activates NF-κB signaling by TLR7 was examined in our next series of experiments. At 24 h after stroke, p-NF-κB was remarkably increased ($p < 0.05$) (Fig. 8A), while decreasing neuronal activity via CNO/hM4Di in MCAO mice significantly down-regulated these p-NF-κB levels ($p < 0.05$) (Fig. 8A). However, in hM3Dq + MCAO mice, CNO had no effect on altering p-NF-κB levels (Fig. 8A). Microglia was stimulated with miR-100-5p mimics or its NC for a period of 48 h. We found that miR-100-5p mimics increased nucleus entry of NF-κB p65, as indicated by immunofluorescence (Fig. 8B). Immunoblotting of the

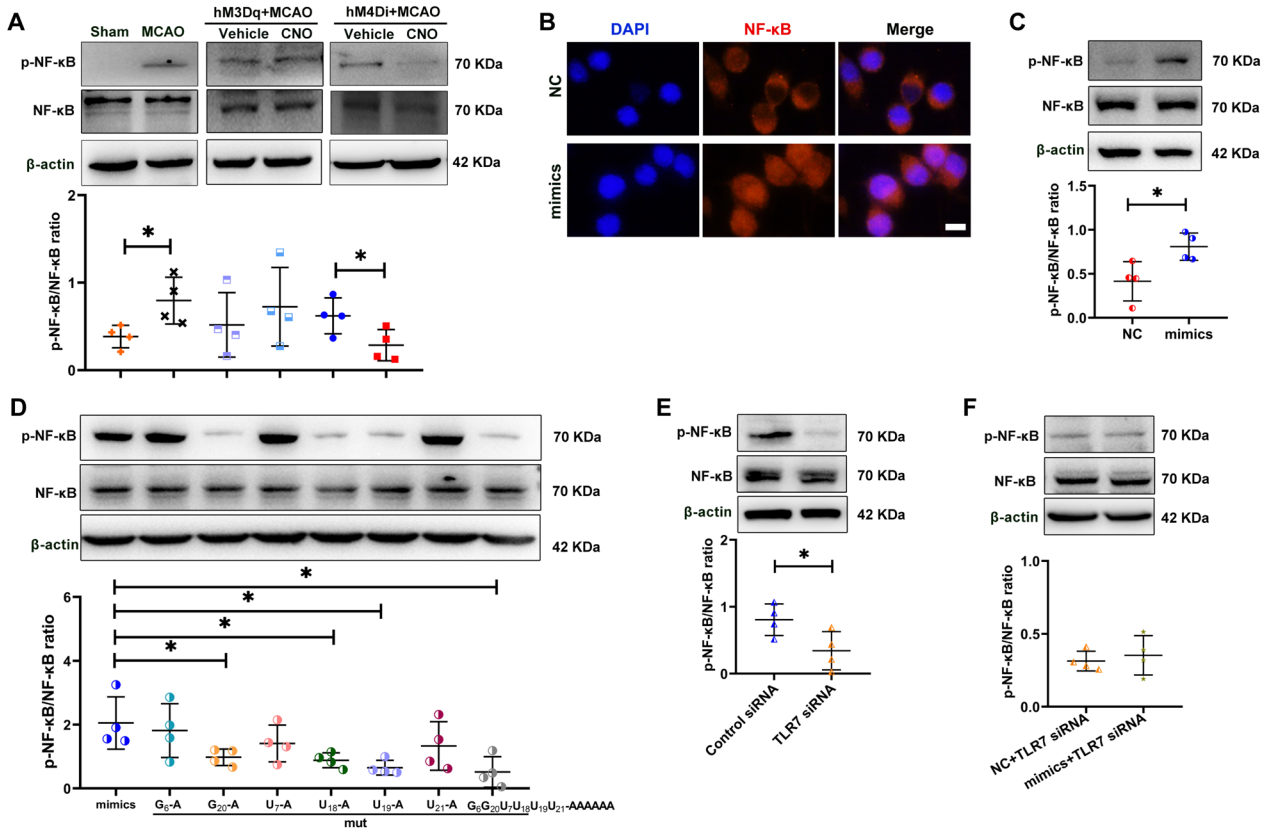

Fig. 8 MiR-100-5p activated NF-κB via TLR7 signaling. **A** Western blot measurements of NF-κB and phosphorylated NF-κB (p-NF-κB) levels in the M1 of each group. N = 4/group. **B** BV-2 cells were treated with 50 nM of miR-100-5p mimics (mimics) and its negative control (NC) for 48 h, then stained with NF-κB (red) and DAPI (blue). Scale bar = 20 μm. **C** BV-2 cells were treated with 50 nM of miR-100-5p mimics (mimics) and its negative control (NC) for 48 h. Then cells were lysed and tested for NF-κB and p-NF-κB. N = 4/group. **D** BV-2 cells were treated with 50 nM of miR-100-5p mimics (mimics) and its mutant for 48 h, cells were lysed and tested for NF-κB and p-NF-κB. N = 4/group. **E** Expression of TLR7 in BV-2 cells was knocked down via siRNA technology. Then, NF-κB and p-NF-κB protein were measured with western blot. The levels of NF-κB and p-NF-κB was quantitated by normalizing to β-actin. N = 4/group. **F** BV-2 cells were transfected with TLR7 siRNA (50 nM) and miR-100-5p mimics (mimics) (50 nM) or its negative control (NC) for 48 h. The levels of NF-κB and p-NF-κB were quantitated by normalizing to β-actin. N = 4/group. All data are represented as mean ± SD. * $p < 0.05$ according to *t*-test except D (mimics vs mut U_{19}-A). * $p < 0.05$ according to Mann–Whitney U test in D (mimics vs mut U_{19}-A)

cell lysates revealed that a strong phosphorylation of p65 was present following treatment with miR-100-5p mimics in BV-2 cells ($p < 0.05$) (Fig. 8C). We also observed that $G_6 \rightarrow A$ or $U_7 \rightarrow A$ mutation in the seed sequence did not affect the expression of p-NF-κB (Fig. 8D), while, either $U_{18} \rightarrow A$ or $U_{19} \rightarrow A$ or $G_{20} \rightarrow A$, but not $U_{21} \rightarrow A$, all within the motif, failed to activate NF-κB. As expected, "U" and "G" mutations to "A" in the seed sequence and motif of miR-100-5p abolished the role of miR-100-5p (Fig. 8D). NF-κB activation appeared to be mediated via TLR7, as TLR7 siRNA microglia failed to respond to miR-100-5p mimics treatment ($p > 0.05$) (Fig. 8E–F).

Inhibiting miR-100-5p reversed neuroinflammation and improved neuronal function following ischemic stroke

To obtain direct evidence that miR-100-5p enriched EVs induced brain damage following stoke, PBS, Nor-N-EVs (2×10^{10} particles/μL, 2 μL) or OGD-N-EVs (2×10^{10} particles/μL, 2 μL) were injected into the M1 to demonstrate the hypothesis that miR-100-5p enriched EVs increased brain injury. We chose a milder form of stress (30 min occlusion) [42, 43] to better distinguish the hypothesized deleterious effects of miR-100-5p increasing on brain damage (Figure S29A). The result showed that treatment with OGD-N-EVs markedly increased expression of miR-100-5p in the M1 at the time of surgery when compared to Nor-N-EVs ($p < 0.01$) (Figure S29B). The behavioral test results showed that the OGD-N-EVs treated mice showed a trend of worsening behavior compared to Nor-N-EVs treated mice in response to ischemic insult, including the mNSS, negative geotaxis test, Kondziella's inverted screen test (Figure S29C-E). OGD-N-EVs led to a greater degree of infarct area as compared to Nor-N-EVs treated mice ($p < 0.05$) (Figure S29F). However, only a single dose of OGD-N-EVs was applied in our experiments, which is one of the reasons why there was no significant difference in behavioral studies. Hence, future studies should be aimed at identifying the optimum dose of OGD-N-EVs delivery and its potential harmful effects in stroke in vivo.

Next, we examined the role of endogenous miR-100-5p in brain injury in vivo by knockdown of miR-100-5p with antagomiR. Mice received unilateral intracerebroventricular stereotaxic microinjection of miR-100-5p^{anta} or control^{anta} and were then subjected to stroke injury 48 h later (Fig. 9A). miR-100-5p^{anta} effectively knocked down miR-100-5p in the M1 and ischemic core of MCAO mice (Fig. 9B). Behavioral performance as measured at 24 h following ischemia indicated that neurological score was significantly reduced in the miR-100-5p^{anta} versus the control^{anta} group ($p < 0.01$, Fig. 9C). Negative geotaxis test results showed that the times involved with turning left or right were significantly reduced in the miR-100-5p^{anta} group, as compared with the control^{anta} group ($p < 0.01$, Fig. 9D). Mice within the miR-100-5p^{anta} group demonstrated enhanced motor coordination as indicated by an increased latency to fall off the rotarod as compared to control^{anta} group ($p < 0.01$) (Fig. 9E).

Mice treated with miR-100-5p^{anta} displayed reduced infarct area compared with miR-100-5p^{anta} group ($p < 0.001$) (Fig. 9F). TUNEL assay results revealed that there was a decrease in apoptotic cell numbers in the miR-100-5p^{anta} group (M1: $p < 0.05$; core: $p < 0.01$) (Fig. 9G). In addition, mice treated with miR-100-5p^{anta} displayed reduced the number of Iba-1^{+} cells compared with control^{anta} group (M1: $p < 0.001$; core: $p < 0.01$) (Fig. 9H). The result of Sholl analysis showed that mice treated with miR-100-5p^{anta} increased the microglia intersection numbers ($p < 0.05$) (Fig. 9J), decreased the area of the microglia cell body ($p < 0.05$) (Fig. 9K), and increased the length of the longest branch compared with control^{anta} group in M1 ($p < 0.05$) (Fig. 9L). In addition, the CD68 staining result showed that a significant decrease in the number of CD68-positive cells in M1 ($p < 0.05$) (Figure S30) of miR-100-5p^{anta} group compare with control^{anta} group. Taken together, inhibiting the

(See figure on next page.)

Fig. 9 Knockdown of miR-100-5p by antagomiR could partially prevented stroke via reducing inflammation and improving organ function. **A** Experimental design. The mice were administered with miR-100-5p antagomiR (miR-100-5p^{anta}) (100 pmol) or the control antagomiR (control^{anta}) via unilateral stereotaxic microinjection into intracerebroventricular 48 h prior to MCAO. Twenty-four hours after MCAO, the mice were behavioral studies, infarction, inflammation and apoptosis examination. i.c.v: intracerebroventricular. **B** Twenty-four hours after MCAO, miR-100-5p abundance was measured in M1 and core with qRT-PCR. N = 4/group. Neurological tests, including mNSS **C**, negative geotaxis test **D**, and Kondziella's inverted screen test **E** were performed in MCAO mice following miR-100-5p^{anta} (100 pmol) or control^{anta} pre-treatment. N = 8/group. **F** Representative TTC staining of brain sections from MCAO mice following miR-100-5p^{anta} or control^{anta} pre-treatment, the infarct area is shown in white. Bar graph shows percentages of infarct area of indicated groups. N = 4/group. **G** Representative TUNEL staining of brain sections from MCAO mice following miR-100-5p^{anta} or control^{anta} pre-treatment. Scale bar = 50 μm. Bar graph shows percentages of apoptosis rate of indicated groups. N = 4/group. **H** Iba-1 staining of brain sections from MCAO mice following miR-100-5p^{anta} or control^{anta} pre-treatment. Scale bar = 25 μm. Bar graph shows the number of Iba-1^{+} cell of indicated groups. N = 4/group. **I** Representative images of Iba1^{+} microglia and the Sholl analysis, the intersection number per radius over the distance from the cell body was displayed graphically in the curve. Scale bar = 10 μm. **J**–**L** The interactions, cell body area and maximum branch length were analyzed. N = 3/group. All data are represented as mean ± SD. * $p < 0.05$, ** $p < 0.01$, *** $p < 0.001$ according to *t*-test except E. ** $p < 0.01$ according to Mann–Whitney U test in E

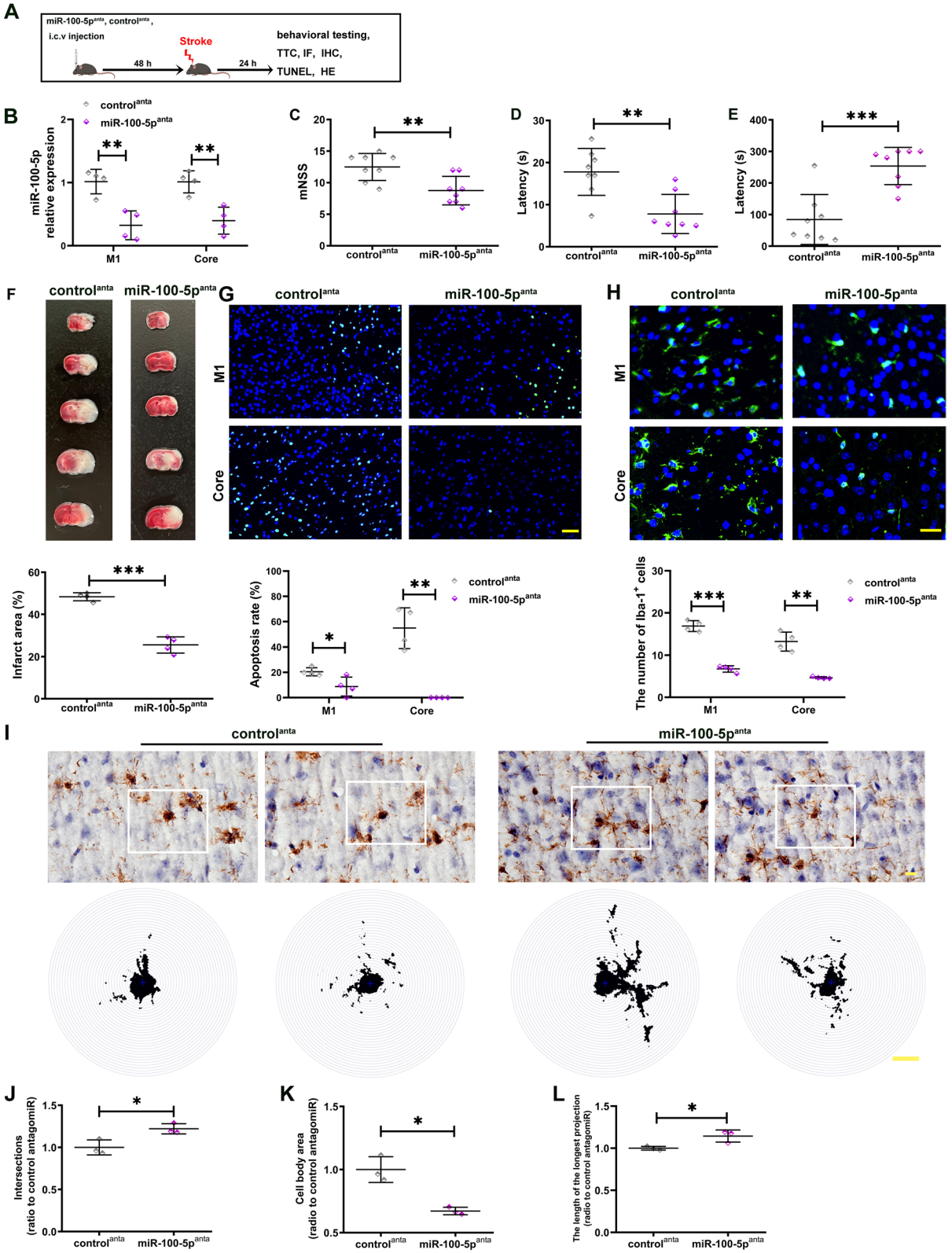

Fig. 9 (See legend on previous page.)

expression of miR-100-5p alleviated the over-activation of microglia in the M1 of MCAO mice. Neither miR-100-5p^{anta} or control^{anta} treatments had any effects on heart, liver, kidney and spleen, while an attenuation in MCAO-induced lung injury was present in the miR-100-5p^{anta} versus the control^{anta} (Figure S31).

Discussion

Our findings emphasized the significance of the increased excitatory and inhibitory neuronal activity in the ipsilesional M1, based on increasing in the number of CaMKIIα$^+$/c-Fos$^+$ and GAD67$^+$/c-Fos$^+$ neurons after cerebral ischemia in mice. The hM4Di-DREADDs-mediated inhibition of M1 neurons effectively alleviated infarct area and neuro-inflammation, along with improving motor performance in these ischemic mice. Mechanistically, miR-100-5p, a highly enriched miRNA in the M1 and M1-EVs within ischemic mice, were highly correlated with stroke severity. EVs from OGD/R-exposed neurons also unregulated miR-100-5p expression and transferred miR-100-5p to microglia to promote acute inflammatory responses by binding to the nucleic acid sensor TLR7 via a $U_{18}U_{19}G_{20}$-containing motif-dependent mechanism. Importantly, these EVs from OGD/R-exposed neurons transferred miR-100-5p to adjacent neurons to further increase neuronal activity and apoptosis by positive feedback, while inhibiting miR-100-5p expression improved poststroke outcomes in MCAO mice. The results of this study suggested that the combination of inhibiting aberrant neuronal activity along with the secretion of specific EVs-miRNAs might serve as novel method for stroke treatment.

Inhibition of M1 neuronal activity restored functional recovery following ischemia

Findings from a number of studies indicate that modulating neuronal activity, such as that achieved using repetitive transcranial magnetic stimulation (rTMS) [44], epidural cortical stimulation [45] and transcranial direct current stimulation [11], have been shown to remap motor and sensory circuits, restore lost functions, and therefore improve the use of paretic limbs. For example, rTMS of ipsilesional M1 can enhance neural plasticity in the motor cortex of chronic stroke patients [44]. Thus, an understanding of neuronal activity in each specific phase and across regions involved with strokes would contribute greatly to our comprehension and treatments of stroke pathophysiology. Interestingly, c-Fos expression is found in OGD/R-exposed neurons in vitro following rTMS treatment [46, 47] and the number of c-Fos$^+$ cells in both affected and unaffected spinal motoneurons was significantly long-term elevated in stroke mice [48]. In rats subjected to cerebral ischemia reperfusion, c-Fos$^+$ neurons were found in the hippocampus and cerebral cortex [49] and neuronal c-Fos levels were increased dramatically following experimentally-induced focal or global cerebral ischemia [50]. Based on the results of flow cytometry analysis and Western blot analysis, we observed similar effects in the current study. First, we showed that the number of CaMKIIα$^+$/c-Fos$^+$ and GAD67$^+$/c-Fos$^+$ neurons remarkably increased within the ipsilesional M1, which were associated with increased levels of c-Fos expression in this region following stroke. Immediate early genes (IEGs) were induced by various forms of brain injury, and their induction was known to be a critical step in programmed cell death [51]. c-Fos (one of IEGs), specifically, was shown to be expressed in a subset of neurons that exhibited condensed chromatin, a hallmark of apoptotic or programmed cell death [52]. As shown in Figure S2 and S4, we can see a significant increase in cell apoptosis and c-Fos in the M1 and infarct core areas after MCAO. In addition, expression of c-Fos became the most widely used functional anatomical marker of activated neurons [53, 54].

Subsequently, we then addressed the issue of whether these ischemic-induced increases in M1 neuronal activity promoted brain damage and neuroinflammation in stroke, and whether pharmacogenetic blocking of this neuronal excitation would restore functional recovery. We found that an injection of CNO into mice expressing hM4Di in the M1 blocked c-Fos expression and c-Fos$^+$/hM4Di$^+$ neurons, demonstrating that this pharmacogenetic manipulation was successful in decreasing M1 neuronal activity. Further, we demonstrated that CNO injection into mice expressing hM4Di in the M1 prevented the neurological impairments and extent of brain infarct area following stroke. This capacity for prevention required a combination of hM4Di expression and CNO injection as brain damage was unaffected in hM4Di + MCAO animals injected with the Vehicle. It was important to note that the injection of CNO in this experiment had no effect on brain injury in hM3Dq + MCAO mice. These results largely agreed with those of previous findings which had reported that an acute inhibition within a subset of excitatory neurons after ischemic stroke could prevent brain injury and improve functional outcomes [7]. Previous studies selective and consecutive only stimulated excitatory neuron in rats [12]. As we found that the number of the CaMKIIα$^+$/c-Fos$^+$ and GAD67$^+$/c-Fos$^+$ neurons was remarkably increased in the ipsilesional M1 in our current study, we chose hSyn-hM4Di to modulate the activity of excitatory and inhibitory neurons in the M1 of MCAO mice. However, it has also been reported that a selective activation of glutamatergic neurons within the M1 promotes functional recovery after ischemic stroke [12]. Results from a

recent study indicated that clozapine-induced excitatory chemogenetic neuromodulation sensory-parietal cortex with hSyn-hM3Dq enhanced motor recovery in a chronic capsular infarct model of stroke [55]. This discrepancy may be attributable to differences in methods used to induce stroke and species used. Factors such as the type and location of stroke (an acute infarct model of stroke as induced by MCAO for our studies versus a chronic capsular infarct model of stroke for Cho et al. [55]) may have contributed to the inconsistent results between the two studies. Moreover, these seemingly contradictory pathological changes might be due to the anatomical and functional heterogeneity of different (excitatory and inhibitory) neurons in M1. When exploring the role of neuronal activity, it is important to know how and why they are produced. If there are several different subsets of neurons leading to different cellular responses, it is essential to distinguish them when estimating the certain pathological changes following stroke. Consequently, further research is necessary to unravel the molecular mechanisms underlying the spatial and temporal patterns of neuronal activity and their associated pathological changes in cellular processes.

Accumulating evidence indicates that injured neurons can influence microglial activation and regulate microglial function. Such activated microglia can produce a disruption of the blood brain barrier to affect neuronal survival via releasing a variety of pro-inflammatory cytokines and toxic substances [56]. Communications between neurons and microglia are bidirectional and often reciprocal, and it seems clear that such cellular interactions rely on the exchange of EVs [57]. For example, microglia-derived EVs stimulate synaptic activity through induction of ceramide and sphingosine synthesis [58]. Neuron-derived EVs have been shown to suppress the activation of M1 microglia and A1 astrocytes, which promotes functional behavioral recovery following spinal cord injury [24], In addition, neuron-derived EVs attenuate LPS-induced microglia activation [25]. In contrast, it has also been reported that neuron-derived EVs containing miR-21-5p promoted proinflammatory activation of microglia and inhibited neurite outgrowth [23]. Here, our current results indicated that small EVs derived from aberrant neuronal activity activated microglia and aggravated inflammation response, as wells as activated neurons in vitro. Importantly, OGD-N-EVs treated mice showed a trend of worsening behavior and exacerbated infracted area after ischemic insult in vivo. Blocking neuronal activity with hM4Di + CNO significantly alleviated neuronal apoptosis and immune responses in the M1 and infracted core after ischemic stroke. Collectively, we speculated that EVs from aberrantly neuronal activity aggravated the pathophysiological processes of stroke, at least in part by inducing neuronal apoptosis and innate immune responses. Therefore, in the early stages of stroke, blocking of the resultant aberrant neuronal activity might serve as an effective intervention for the treatment of ischemic stroke.

Aberrant neuronal activity altered the expression of EVs-miRNA and in turn aggravated neuronal activity and microglial activation

MiRNAs have been recognized as playing a critical role in the interplay between neuron and glia cells through a variety of intracellular signaling pathways as well as through paracrine effects via EVs. Therefore, we next determined whether neuronal activity altered EVs-miRNA. MiR-100-5p belongs to the miR-99 family, which consists of three members, miR-99a, miR-99b, and miR-100. It has been reported that the miR-99 family is involved in regulating cell survival, cell stress responses, proliferation, angiogenesis, DNA damage, and wound healing processes [59, 60]. MiR-100-5p is upregulated in the frontal gyrus and cerebellum of Alzheimer's disease patients [61] and plays a predominant role in Aβ-induced neuronal pathologies [62]. In addition, miR-100-5p release from EVs has also been implicated in multiple inflammatory pathologies related to atherosclerosis [63], autoimmune dacryoadenitis [64], temporomandibular joint chondrocytes [65] and osteoarthritis [66]. Interestingly, Thomas et al. reported that miR-100-5p released from apoptotic cortical neurons contributed to microglia activation and neuronal apoptosis [37]. However, whether miR-100-5p-rich EVs play a role in the interplay between neurons and glia cells as related to ischemia is not clear. In this study, increased levels of miR-100-5p were observed in the M1 of MCAO mice and OGD/R-exposed neurons, as well as in EVs derived from M1 and OGD/R-exposed neurons. Increases in neuronal activity, as achieved with hM3Dq-plasmid + CNO, also promoted miR-100-5p expression in neurons. Based on these findings, we speculated that ischemia-evoked neuronal activity would upregulate miR-100-5p expression of neurons and, in this way, generated more miR-100-5p loading into EVs. We found that miR-100-5p-rich EVs can be transported into microglia and neurons, resulting in inflammatory responses and neuronal apoptosis as demonstrated in vitro. Overexpression of miR-100-5p within neurons further increased neuronal activity and apoptosis through a positive feedback loop and there existed a high correlation between the miR-100-5p levels of M1-EVs or M1 and infarct area within the brain of MCAO mice. A loss of miR-100-5p function within ischemic mice improved their poststroke outcomes. Similarly, recent findings from other investigators have also suggested that lower miR-100-5p levels in circulating EVs

appear to be related to improvements of patients with ischaemic stroke [67]. Taken together, these data support the hypothesis that miR-100-5p in EVs play an important role in stroke pathogenesis. Moreover, to the best of our knowledge our findings represented the first demonstration that EVs resulting from aberrant neuronal activity, possessed higher loading levels of miR-100-5p, which can elicit distinct downstream events (described below). Accordingly, manipulations involved in altering the combination of miRNAs and neuron-derived EVs might provide a minimally invasive approach for the treatment of ischemic stroke.

MiR-100-5p directly activated the TLR signaling pathway

TLR is a pivotal component of host innate immune defense mechanisms and plays a critical role in CNS injury, not only by triggering inflammatory responses, but also by mediating cell autonomous damage [68]. Emerging evidence has been demonstrated that TLR, particularly endosomal TLR7, can be activated by miRNAs within the CNS [37, 69]. Mature miRNAs with GU-rich sequences also contribute to immune stimulation by serving as physiological ligands for murine TLR7 and human TLR8 [39]. As one example, extracellular let-7b can serve as a potent activator of TLR7 signaling in neurons, leading to neurodegeneration [38]. Fabbri et al. reported that miRNAs can bind to human TLR8 and murine TLR7 and certain nucleotides in specific positions of the miRNA sequence affected the activation of TLR [70]. Extracellular miR-146a-5p acts as an innate immune effector driving acute inflammatory response by binding to the nucleic acid sensor TLR7 via a UU-containing motif-dependent mechanism [69]. Interestingly, miR-100-5p can act as an endogenous TLR7 and activates microglia, but it lacks the interacting motif needed to activate the respective TLR7 [37]. Using a computer predictive algorithm and a series of single U/A and or G/A mutations in the miR-100-5p molecule, we identified an essential role for the successive $U_{18}U_{19}G_{20}$ in the $U_{18}U_{19}G_{20}U_{21}$ motif for miR-100-5p-mediated cellular cytokine responses. Moreover, we demonstrated a physical association between miR-100-5p and TLR7 in cells expressing TLR7 and the necessity of TLR7 in miR-100-5p-induced neurotoxicity in microglia and neuron. Our study showed that overexpression of miR-100-5p induced an increase in c-Fos expression in neurons, suggesting that miR-100-5p induces neuronal activation. The previous reported that c-Fos proteins were induced by TLR7 activation in cultured neurons [71]. Combined with our study results, we found that miR-100-5p can bind to and activate TLR7 through $U_{18}U_{19}G_{20}$-motif, so we speculated that miR-100-5p and its $U_{18}U_{19}G_{20}$-motif might induce c-Fos expression and neuron activation through binding and activating TLR7, ultimately leading to a decrease in neuronal activity.

Downstream mechanisms of TLR7 are known to involve the activation of NF-κB pathways [72]. The transcription factor, NF-κB plays a critical role in inflammation, cell proliferation and cell apoptosis [73] and TLR7 agonists are reported to induce NF-κB activation in myeloid cells [41]. Moreover, results from a recent study have revealed that activated TLR7 enhances the MyD88/NF-κB cascade in murine macrophages, ultimately leading to inflammation [74]. From our analysis, we found that there is an increased expression in p-NF-κB levels and NF-κB nuclear translocation in microglia following extracellular miR-100-5p treatment. Findings from in vitro model also showed that a TLR7 deficiency ameliorated miR-100-5p-mediated NF-κB levels and IL-1β production. In addition, we found that hM4Di + CNO or miR-100-5p^{anta} treatment improved ischemia-induced lung injury. Previous studies found that stroke-induced pathophysiology can include increases in peripheral inflammation, which greatly increases the risk of peripheral organ infection and aggravates organ damage [75–77]. NF-κB pathway is involved in the inhibition of stroke-induced lung injury. For example, p-NF-κB in the mice lung was significantly increased after MCAO. Activation of the NF-κB pathway in lung was also suppressed after the degree of lung injury was relieved following a reduction in cerebral infarct volume [78]. Our study showed that neuroinflammation and p-NF-κB in the brain were significantly inhibited after hM4Di + CNO or miR-100-5p^{anta} treatment. hM4Di + CNO or miR-100-5p^{anta} treatment not only has a protective effect against brain injury but also improves lung injury. Through our results and previous studies, we hypothesized that this phenomenon might be due to improvements in lung immunosuppression after stroke remission, thus reducing infection in the lung. However, the precise mechanisms by which cerebral ischemia affects lung immunity remain to be investigated. Altogether, extracellular miR-100-5p seemed to play an important role in innate immune cell activation via the TLR7-NF-κB signaling pathway.

The present study has a number limitations that may decrease some of its implications as related to stroke. First, for technical reasons we could not sort EVs from neurons in vivo and clarify their role in the brain. In this report, we used OGD/R-exposed neurons in vitro to model ishemia-evoked neuronal activity and collected EVs from these neurons to investigate the resultant effects on brain immune responses as determined in vitro. Such an in vitro analysis of OGD/R-exposed neurons may not fully replicate the changes observed in M1 neurons of MCAO mice. Consequently, the mechanisms of EVs and means through which they may modulate mciroglial

and neuronal function activity may differ between these in vitro versus in vivo models. Nonetheless, the data presented here establish models through which such modulatory mechanisms can be further investigated. Second, although at the acute time point selected in these experiments, the microglial activition was mainly attributable to their responses of the brain injury itself, it may also be possible that EVs from ischemic-evoked neuronal activity can specifically affect microglial activation.Third, no in vivo experiments utilizing miR-100-5p knockout mice were performed. This deficit is mostly due to time constraints and resource scarcity of such mice that possess this neuron specific miR-100-5p deletion. Therefore, we used miR-100-5p^{anta} in mice as an approach to investigate this possibility. Fourth, in vitro experiments, we found no elevated expression of miR-100-5p in glia cells and postulated that neurons were the local source of miR-100-5p following ischemic stroke. However, in an in vivo setting this particular miRNA might also be derived from endothelial cells or infiltrating inflammatory cells. Therefore, current research suggested that ischemic stroke might alter the composition of neuronal EVs, thereby exacerbating damage.

Conclusion

In the present study, we demonstrated that ischemic stroke was associated with increased neuronal activity in the M1 as determined using both in vivo and in vitro models. Aberrant neuronal activity generated unique small EVs which activated local neurons and microglia in response to ischemic stroke. EVs-miR-100-5p aggravated neurotoxicity via $U_{18}U_{19}G_{20}$-motif binding and activating TLR7/NF-κB signaling pathway after stroke. Based on these findings, the potential of using a combination of agents capable of inhibiting aberrant neuronal activity and the secretion of specific EVs-miRNAs may serve as a novel and efficacious protocols in the treatment of strokes.

Abbreviations

AAV	Adeno-associated virus
Arg-1	Arginase-1
CaMKII	Calcium/calmodulin-dependent protein kinase II
CNS	Central nervous system
CNO	Clozapine-N-oxide
IP	Immunoprecipitation
DAPI	4′,6′-Diamidino-2-phenylindole dihydrochloride hydrate
DREADDs	Designer Receptors Exclusively Activated by Designer Drugs
DMSO	Dimethyl sulfoxide
EVs	Extracellular vesicles
FACS	Fluorescence activated cell sorting
FAM	5-Carboxyfluorescein
FBS	Fetal bovine serum
GAD	Glutamate decarboxylase
HE	Hematoxylin Eosin
IL-1β	Interleukin 1β
IL-6	Interleukin 6
i.p.	Intraperitoneal
LPS	Lipopolysaccharide
MCAO	Middle cerebral artery occlusion
mNSS	Modified neurological severity score
M1	Primary motor cortex
NF-κB	Nuclear factor-κB
OCT	Optimal cutting temperature compound
OGD/R	Oxygen–glucose deprivation/reoxygenation
RIP	RNA immunoprecipitation
rTMS	Repetitive transcranial magnetic stimulation
SD	Standard deviation
TLR	Toll like receptor
TEM	Transmission electron microscopy
TNF-α	Tumor necrosis factor α

Supplementary Information

The online version contains supplementary material available at https://doi.org/10.1186/s12951-024-02782-0.

Supplementary Material 1

Acknowledgements

We are grateful to Dr. Yan Li (the First Affiliated Hospital of Shandong First Medical University and Shandong Provincial Qianfoshan Hospital) for the patch-clamp assay. We thank Translational Medicine Core Facility of Shandong University for consultation and instrument availability that supported this work.

Author contributions

Zhen Wang: Conceptualization, Investigation, Resources, Writing-Original Draf, Writing-Review&Editing, Visualization, Supervision, Project administration and Funding acquisition. Danqing Xin: Formal analysis, Methodology, Investigation, Visualization, Data Curation and Writing-Review&Editing. Tingting Li and Zhaoyi Jing: Methodology and Writing-Review&Editing. Xiao fan Guo: Conceptualization. Chengcheng Gai, Yahong Cheng, Zige Jang, Qian Luo, Shuwen Yu, Jiao Cheng and Bing Gu: Methodology. Dexiang Liu: Supervision, Writing-Review&Editing and Data Curation. All authors have read and approved the final manuscript. All authors reviewed the manuscript.

Funding

Research funding support for this work was from the National Natural Science Foundation of China (No. 82271327, 82072535 and 81873768) to Dr. Zhen Wang.

Availability of data and materials

No datasets were generated or analysed during the current study.

Declarations

Ethics approval and consent to participate

All animal care and experimental procedures were conducted in accordance with the guidance of the Care and Use of Laboratory Animals from the National Institutes of Health and were approved by the Laboratory Animal Ethics Committee of Shandong University (approval No. ECSBMSSDU2022-2–52).

Consent for publication

Not applicable.

Competing interests

The authors declare no competing interests.

Author details

[1]Department of Physiology, School of Basic Medical Sciences, Cheeloo College of Medicine, Shandong University, 44 Wenhua Xi Road, Jinan, Shandong 250012, People's Republic of China. [2]Department of Neurology, Loma Linda University Health, Loma Linda, CA 92354, USA. [3]Department of Medical Psychology and Ethics, School of Basic Medicine Sciences, Cheeloo College

of Medicine, Shandong University, Jinan, Shandong 250012, People's Republic of China.

Received: 22 March 2024 Accepted: 16 August 2024
Published online: 03 September 2024

References

1. George PM, Steinberg GK. Novel stroke therapeutics: unraveling stroke pathophysiology and its impact on clinical treatments. Neuron. 2015;87:297–309.
2. Hartings JA, Rolli ML, Lu X-CM, Tortella FC. Delayed secondary phase of peri-infarct depolarizations after focal cerebral ischemia: relation to infarct growth and neuroprotection. J Neurosci. 2003;23:11602–10.
3. Chamorro Á, Dirnagl U, Urra X, Planas AM. Neuroprotection in acute stroke: targeting excitotoxicity, oxidative and nitrosative stress, and inflammation. Lancet Neurol. 2016;15:869–81.
4. von Bornstädt D, Houben T, Seidel JL, Zheng Y, Dilekoz E, Qin T, et al. Supply-demand mismatch transients in susceptible peri-infarct hot zones explain the origins of spreading injury depolarizations. Neuron. 2015;85:1117–31.
5. Hossmann KA. Periinfarct depolarizations. Cerebrovasc Brain Metab Rev. 1996;8:195–208.
6. Xia X, Chen J, Ren H, Zhou C, Zhang Q, Cheng H, et al. Gypenoside pretreatment alleviates the cerebral ischemia injury via inhibiting the microglia-mediated neuroinflammation. Mol Neurobiol. 2023. https://doi.org/10.1007/s12035-023-03624-0.
7. Wang Y-C, Galeffi F, Wang W, Li X, Lu L, Sheng H, et al. Chemogenetics-mediated acute inhibition of excitatory neuronal activity improves stroke outcome. Exp Neurol. 2020;326: 113206.
8. Caracciolo L, Marosi M, Mazzitelli J, Latifi S, Sano Y, Galvan L, et al. CREB controls cortical circuit plasticity and functional recovery after stroke. Nat Commun. 2018;9:2250.
9. Carmichael ST. Emergent properties of neural repair: elemental biology to therapeutic concepts. Ann Neurol. 2016;79:895–906.
10. Di Pino G, Pellegrino G, Assenza G, Capone F, Ferreri F, Formica D, et al. Modulation of brain plasticity in stroke: a novel model for neurorehabilitation. Nat Rev Neurol. 2014;10:597–608.
11. Rivera-Urbina GN, Batsikadze G, Molero-Chamizo A, Paulus W, Kuo M-F, Nitsche MA. Parietal transcranial direct current stimulation modulates primary motor cortex excitability. Eur J Neurosci. 2015;41:845–55.
12. Hu K-H, Li Y-A, Jia W, Wu G-Y, Sun L, Wang S-R, et al. Chemogenetic activation of glutamatergic neurons in the motor cortex promotes functional recovery after ischemic stroke in rats. Behav Brain Res. 2019;359:81–8.
13. Cheng MY, Wang EH, Woodson WJ, Wang S, Sun G, Lee AG, et al. Optogenetic neuronal stimulation promotes functional recovery after stroke. Proc Natl Acad Sci U S A. 2014;111:12913–8.
14. Clarkson AN, Huang BS, Macisaac SE, Mody I, Carmichael ST. Reducing excessive GABA-mediated tonic inhibition promotes functional recovery after stroke. Nature. 2010;468:305–9.
15. Théry C, Witwer KW, Aikawa E, Alcaraz MJ, Anderson JD, Andriantsitohaina R, et al. Minimal information for studies of extracellular vesicles 2018 (MISEV2018): a position statement of the international society for extracellular vesicles and update of the MISEV2014 guidelines. J Extracell Vesicles. 2018;7:1535750.
16. Jia Y, Yu L, Ma T, Xu W, Qian H, Sun Y, et al. Small extracellular vesicles isolation and separation: current techniques, pending questions and clinical applications. Theranostics. 2022;12:6548–75.
17. Mathieu M, Martin-Jaular L, Lavieu G, Théry C. Specificities of secretion and uptake of exosomes and other extracellular vesicles for cell-to-cell communication. Nat Cell Biol. 2019;21:9–17.
18. Song Y, Li Z, He T, Qu M, Jiang L, Li W, et al. M2 microglia-derived exosomes protect the mouse brain from ischemia-reperfusion injury via exosomal miR-124. Theranostics. 2019;9:2910–23.
19. Deng Z, Wang J, Xiao Y, Li F, Niu L, Liu X, et al. Ultrasound-mediated augmented exosome release from astrocytes alleviates amyloid-β-induced neurotoxicity. Theranostics. 2021;11:4351–62.
20. Chiang C-S, Fu S-J, Hsu C-L, Jeng C-J, Tang C-Y, Huang Y-S, et al. Neuronal exosomes secreted under oxygen-glucose deprivation/reperfusion presenting differentially expressed mirnas and affecting neuronal survival and neurite outgrowth. Neuromolecular Med. 2021;23:404–15.
21. Wilton DK, Dissing-Olesen L, Stevens B. Neuron-glia signaling in synapse elimination. Annu Rev Neurosci. 2019;42:107–27.
22. Frühbeis C, Fröhlich D, Kuo WP, Amphornrat J, Thilemann S, Saab AS, et al. Neurotransmitter-triggered transfer of exosomes mediates oligodendrocyte-neuron communication. PLoS Biol. 2013;11: e1001604.
23. Yin Z, Han Z, Hu T, Zhang S, Ge X, Huang S, et al. Neuron-derived exosomes with high miR-21-5p expression promoted polarization of M1 microglia in culture. Brain Behav Immun. 2020;83:270–82.
24. Jiang D, Gong F, Ge X, Lv C, Huang C, Feng S, et al. Neuron-derived exosomes-transmitted miR-124-3p protect traumatically injured spinal cord by suppressing the activation of neurotoxic microglia and astrocytes. J Nanobiotechnology. 2020;18:105.
25. Peng H, Harvey BT, Richards CI, Nixon K. Neuron-derived extracellular vesicles modulate microglia activation and function. Biology (Basel). 2021;10:948.
26. Fauré J, Lachenal G, Court M, Hirrlinger J, Chatellard-Causse C, Blot B, et al. Exosomes are released by cultured cortical neurones. Mol Cell Neurosci. 2006;31:642–8.
27. Han M, Cao Y, Xue H, Chu X, Li T, Xin D, et al. Neuroprotective effect of mesenchymal stromal cell-derived extracellular vesicles against cerebral ischemia-reperfusion-induced neural functional injury: a pivotal role for AMPK and JAK2/STAT3/NF-κB Signaling pathway modulation. Drug Des Devel Ther. 2020;14:2865–76.
28. Kim H, Seo JS, Lee S-Y, Ha K-T, Choi BT, Shin Y-I, et al. AIM2 inflammasome contributes to brain injury and chronic post-stroke cognitive impairment in mice. Brain Behav Immun. 2020;87:765–76.
29. Chen J, Sanberg PR, Li Y, Wang L, Lu M, Willing AE, et al. Intravenous administration of human umbilical cord blood reduces behavioral deficits after stroke in rats. Stroke. 2001;32:2682–8.
30. Ridder K, Sevko A, Heide J, Dams M, Rupp A-K, Macas J, et al. Extracellular vesicle-mediated transfer of functional RNA in the tumor microenvironment. Oncoimmunology. 2015;4: e1008371.
31. Tian Y, Gong M, Hu Y, Liu H, Zhang W, Zhang M, et al. Quality and efficiency assessment of six extracellular vesicle isolation methods by nano-flow cytometry. J Extracell Vesicles. 2020;9:1697028.
32. Xin D, Li T, Chu X, Ke H, Liu D, Wang Z. MSCs-extracellular vesicles attenuated neuroinflammation, synapse damage and microglial phagocytosis after hypoxia-ischemia injury by preventing osteopontin expression. Pharmacol Res. 2021;164: 105322.
33. Brewer HB, Ronan R, Meng M, Bishop C. Isolation and characterization of apolipoproteins A-I, A-II, and A-IV. Methods Enzymol. 1986;128:223–46.
34. Rubio FJ, Li X, Liu Q-R, Cimbro R, Hope BT. Fluorescence activated cell sorting (FACS) and gene expression analysis of Fos-expressing neurons from fresh and frozen rat brain tissue. J Vis Exp. 2016. https://doi.org/10.3791/54358-v.
35. Rubio FJ, Liu Q-R, Li X, Cruz FC, Leão RM, Warren BL, et al. Context-induced reinstatement of methamphetamine seeking is associated with unique molecular alterations in Fos-expressing dorsolateral striatum neurons. J Neurosci. 2015;35:5625–39.
36. Slepko N, Levi G. Progressive activation of adult microglial cells in vitro. Glia. 1996;16:241–6.
37. Wallach T, Mossmann ZJ, Szczepek M, Wetzel M, Machado R, Raden M, et al. MicroRNA-100-5p and microRNA-298-5p released from apoptotic cortical neurons are endogenous Toll-like receptor 7/8 ligands that contribute to neurodegeneration. Mol Neurodegener. 2021;16:80.
38. Lehmann SM, Krüger C, Park B, Derkow K, Rosenberger K, Baumgart J, et al. An unconventional role for miRNA: let-7 activates Toll-like receptor 7 and causes neurodegeneration. Nat Neurosci. 2012;15:827–35.
39. Zhang Z, Ohto U, Shibata T, Taoka M, Yamauchi Y, Sato R, et al. Structural analyses of toll-like receptor 7 reveal detailed rna sequence specificity and recognition mechanism of agonistic ligands. Cell Rep. 2018;25:3371-3381.e5.
40. Nazmi A, Mukherjee S, Kundu K, Dutta K, Mahadevan A, Shankar SK, et al. TLR7 is a key regulator of innate immunity against Japanese encephalitis virus infection. Neurobiol Dis. 2014;69:235–47.
41. Eng H-L, Hsu Y-Y, Lin T-M. Differences in TLR7/8 activation between monocytes and macrophages. Biochem Biophys Res Commun. 2018;497:319–25.

42. Ahn JH, Song M, Kim H, Lee T-K, Park CW, Park YE, et al. Differential regional infarction, neuronal loss and gliosis in the gerbil cerebral hemisphere following 30 min of unilateral common carotid artery occlusion. Metab Brain Dis. 2019;34:223–33.
43. Park JH, Cho JH, Ahn JH, Choi SY, Lee T-K, Lee J-C, et al. Neuronal loss and gliosis in the rat striatum subjected to 15 and 30 minutes of middle cerebral artery occlusion. Metab Brain Dis. 2018;33:775–84.
44. Lefaucheur J-P, André-Obadia N, Antal A, Ayache SS, Baeken C, Benninger DH, et al. Evidence-based guidelines on the therapeutic use of repetitive transcranial magnetic stimulation (rTMS). Clin Neurophysiol. 2014;125:2150–206.
45. Levy RM, Harvey RL, Kissela BM, Winstein CJ, Lutsep HL, Parrish TB, et al. Epidural electrical stimulation for stroke rehabilitation: results of the prospective, multicenter, randomized single-blinded everest trial. Neurorehabil Neural Repair. 2016;30:107–19.
46. Roque C, Pinto N, Vaz Patto M, Baltazar G. Astrocytes contribute to the neuronal recovery promoted by high-frequency repetitive magnetic stimulation in in vitro models of ischemia. J Neurosci Res. 2021;99:1414–32.
47. Gava-Junior G, Ferreira SA, Roque C, Mendes-Oliveira J, Serrenho I, Pinto N, et al. High-frequency repetitive magnetic stimulation rescues ischemia-injured neurons through modulation of glial-derived neurotrophic factor present in the astrocyte's secretome. J Neurochem. 2023;164:813–28.
48. Lee S, Toda T, Kiyama H, Yamashita T. Weakened rate-dependent depression of Hoffmann's reflex and increased motoneuron hyperactivity after motor cortical infarction in mice. Cell Death Dis. 2014;5: e1007.
49. Zhang H, Li L, Xu G-Y, Mei Y-W, Zhang J-J, Murong S-X, et al. Changes of c-fos, malondialdehyde and lactate in brain tissue after global cerebral ischemia under different brain temperatures. J Huazhong Univ Sci Technolog Med Sci. 2014;34:354–8.
50. Uemura Y, Kowall NW, Moskowitz MA. Focal ischemia in rats causes time-dependent expression of c-fos protein immunoreactivity in widespread regions of ipsilateral cortex. Brain Res. 1991;552:99–105.
51. Estus S, Zaks WJ, Freeman RS, Gruda M, Bravo R, Johnson EM. Altered gene expression in neurons during programmed cell death: identification of c-jun as necessary for neuronal apoptosis. J Cell Biol. 1994;127:1717–27.
52. Estus S, Tucker HM, van Rooyen C, Wright S, Brigham EF, Wogulis M, et al. Aggregated amyloid-beta protein induces cortical neuronal apoptosis and concomitant "apoptotic" pattern of gene induction. J Neurosci. 1997;17:7736–45.
53. Hoffman GE, Smith MS, Verbalis JG. c-Fos and related immediate early gene products as markers of activity in neuroendocrine systems. Front Neuroendocrinol. 1993;14:173–213.
54. Kovács KJ. Measurement of immediate-early gene activation- c-fos and beyond. J Neuroendocrinol. 2008;20:665–72.
55. Cho J, Ryu S, Lee S, Kim J, Park J-Y, Kwon H-S, et al. Clozapine-induced chemogenetic neuromodulation rescues post-stroke deficits after chronic capsular infarct. Transl Stroke Res. 2023;14:499–512.
56. Norris GT, Smirnov I, Filiano AJ, Shadowen HM, Cody KR, Thompson JA, et al. Neuronal integrity and complement control synaptic material clearance by microglia after CNS injury. J Exp Med. 2018;215:1789–801.
57. Frühbeis C, Fröhlich D, Kuo WP, Krämer-Albers E-M. Extracellular vesicles as mediators of neuron-glia communication. Front Cell Neurosci. 2013;7:182.
58. Antonucci F, Turola E, Riganti L, Caleo M, Gabrielli M, Perrotta C, et al. Microvesicles released from microglia stimulate synaptic activity via enhanced sphingolipid metabolism. EMBO J. 2012;31:1231–40.
59. Mueller AC, Sun D, Dutta A. The miR-99 family regulates the DNA damage response through its target SNF2H. Oncogene. 2013;32:1164–72.
60. Jin Y, Tymen SD, Chen D, Fang ZJ, Zhao Y, Dragas D, et al. MicroRNA-99 family targets AKT/mTOR signaling pathway in dermal wound healing. PLoS ONE. 2013;8: e64434.
61. Cogswell JP, Ward J, Taylor IA, Waters M, Shi Y, Cannon B, et al. Identification of miRNA changes in Alzheimer's disease brain and CSF yields putative biomarkers and insights into disease pathways. J Alzheimers Dis. 2008;14:27–41.
62. Ye X, Luo H, Chen Y, Wu Q, Xiong Y, Zhu J, et al. MicroRNAs 99b–5p/100-5p regulated by endoplasmic reticulum stress are involved in abeta-induced pathologies. Front Aging Neurosci. 2015;7:210.
63. Gao H, Yu Z, Li Y, Wang X. miR-100-5p in human umbilical cord mesenchymal stem cell-derived exosomes mediates eosinophilic inflammation to alleviate atherosclerosis via the FZD5/Wnt/β-catenin pathway. Acta Biochim Biophys Sin (Shanghai). 2021;53:1166–76.
64. Li N, Gao Z, Zhao L, Du B, Ma B, Nian H, et al. MSC-derived small extracellular vesicles attenuate autoimmune dacryoadenitis by promoting M2 macrophage polarization and inducing tregs via miR-100-5p. Front Immunol. 2022;13: 888949.
65. Luo P, Jiang C, Ji P, Wang M, Xu J. Exosomes of stem cells from human exfoliated deciduous teeth as an anti-inflammatory agent in temporomandibular joint chondrocytes via miR-100-5p/mTOR. Stem Cell Res Ther. 2019;10:216.
66. Li K, Yan G, Huang H, Zheng M, Ma K, Cui X, et al. Anti-inflammatory and immunomodulatory effects of the extracellular vesicles derived from human umbilical cord mesenchymal stem cells on osteoarthritis via M2 macrophages. J Nanobiotechnology. 2022;20:38.
67. Otero-Ortega L, Alonso-López E, Pérez-Mato M, Laso-García F, Gómez-de Frutos MC, Diekhorst L, et al. Circulating extracellular vesicle proteins and microrna profiles in subcortical and cortical-subcortical ischaemic stroke. Biomedicines. 2021;9:786.
68. Heil F, Hemmi H, Hochrein H, Ampenberger F, Kirschning C, Akira S, et al. Species-specific recognition of single-stranded RNA via toll-like receptor 7 and 8. Science. 2004;303:1526–9.
69. Wang S, Yang Y, Suen A, Zhu J, Williams B, Hu J, et al. Role of extracellular microRNA-146a-5p in host innate immunity and bacterial sepsis. Iscience. 2021;24:103441.
70. Fabbri M, Paone A, Calore F, Galli R, Gaudio E, Santhanam R, et al. MicroRNAs bind to Toll-like receptors to induce prometastatic inflammatory response. Proc Natl Acad Sci U S A. 2012;109:E2110-2116.
71. Liu H-Y, Hong Y-F, Huang C-M, Chen C-Y, Huang T-N, Hsueh Y-P. TLR7 negatively regulates dendrite outgrowth through the Myd88-c-Fos-IL-6 pathway. J Neurosci. 2013;33:11479–93.
72. Sun S, Rao NL, Venable J, Thurmond R, Karlsson L. TLR7/9 antagonists as therapeutics for immune-mediated inflammatory disorders. Inflamm Allergy Drug Targets. 2007;6:223–35.
73. Dixit V, Mak TW. NF-kappaB signaling Many roads lead to madrid. Cell. 2002;111:615–9.
74. Tang J, Cheng X, Yi S, Zhang Y, Tang Z, Zhong Y, et al. Euphorbia factor L2 ameliorates the progression of K/BxN serum-induced arthritis by blocking TLR7 mediated IRAK4/IKKβ/IRF5 and NF-kB signaling pathways. Front Pharmacol. 2021;12: 773592.
75. Wang J, Zhang J, Ye Y, Xu Q, Li Y, Feng S, et al. Peripheral organ injury after stroke. Front Immunol. 2022;13: 901209.
76. Kerr N, de Rivero Vaccari JP, Dietrich WD, Keane RW. Neural-respiratory inflammasome axis in traumatic brain injury. Exp Neurol. 2020;323: 113080.
77. Kerr NA, de Rivero Vaccari JP, Abbassi S, Kaur H, Zambrano R, Wu S, et al. Traumatic brain injury-induced acute lung injury: evidence for activation and inhibition of a neural-respiratory-inflammasome axis. J Neurotrauma. 2018;35:2067–76.
78. Xu Q, Ye Y, Wang Z, Zhu H, Li Y, Wang J, et al. NLRP3 knockout protects against lung injury induced by cerebral ischemia-reperfusion. Oxid Med Cell Longev. 2022;2022:6260102.

Publisher's Note